Dear Editor,

We would like to thank the two referees for their comments and suggestions to improve the quality of our manuscript “The Beijing Climate Center Climate System Model (BCC-CSM): Main Progress from CMIP5 to CMIP6” by Tongwen Wu et al. Following their suggestions, we added 5 further figures in the revised manuscript. So, all figures in the first manuscript are renumbered. We have also changed the order of presentation for some subsections in Section 4 (Results). The point-to-point response to referees’ comments are enclosed in the following.

Best regards,

Tongwen Wu and all co-authors

==========

**Response to Anonymous Referee #1**

**General comments:**

**In this article the authors describe the changes from the BCC-CSM1.1 model that was used in CMIP5 to the new BCC-CSM2 model that is now employed in CMIP6. They compare the "historical" simulations as specified by CMIP5 and CMIP6, respectively, of the old and new model. They show that the new model can simulate the mean climate as well as some modes of variability with some skill, and they point out a number of improvements in the new simulation compared to the old one. Obviously this article is meant to be a basic, citable documentation for the new CMIP6 simulations of the BCC-CSM2 model.**

**The documentation and analysis of the simulations is superficial. No attempt is taken to describe or analyze the effects of the single model improvements, or to attribute the identified differences between the two simulations to the introduced model changes. Therefore there is not much that the reader can learn from this article, except that the coupled model can reproduce the transient climate of the CMIP historical experiment with some skill. The authors point at future publications ("to be submitted") for other experiments, model resolutions or the QBO in the historical simulations.**

**Response**:

Thanks for the relevant comments. Yes, the purpose of this manuscript is to document the transition of our model BCC-CSM from CMIP5 to CMIP6. We hope that it can be a reference for the different experiments of CMIP6 which are progressively available (or very soon for some specific runs) for the scientific community of CMIP6. So we compare here only the general performance between our old and new models, particular performance being investigated in detail in other specific papers. Nevertheless, we think that it is useful to add some more materials (including 5 new illustrations), which goes to the general sense of both Reviewers.

**L40: …Many climate models in the world have been developed since the IPCC-AR4 …The IPCC reports certainly motivated many groups to contribute climate projections for the assessment of future climates, for which these groups developed suitable models. But I do not see why IPCC-AR4 is pointed out as a special landmark along the path of the development of global climate models or Earth system models. Rather the initial coupled model inter-comparison project (CMIP) would deserve to be mentioned, and the way the CMIPs were developed by the community and the working group on coupled modeling (WGCM).**

**Response**: We agree that CMIP and its promoter WGCM played an important role for climate modelling in the world. They should be more acknowledged than IPCC. The latter is however much more popular for a general public.

**L71: … Its performance is presented in a separated paper (Wu et al., to be submitted).**

**… Please check if references to "to be submitted" articles are allowed in GMDD. Better write "… Its performance will be presented in a separate paper. ...".**

**Response**: Proposition relevant and accepted.

**L78: Please include a figure that compares the profiles of layer thickness against the height of the layer for the L26 and L46 grids, using for example a simple log-p height definition. This would clarify how the vertical resolution has been improved.**

**Response**: We added Figure 1 in the revised manuscript to show the profiles of layer thickness against the height for 26 vertical layers in BCC-CSM-1.1m and 46 vertical layers in BCC-CSM2-MR.

**L81: 2.1 Atmospheric component BCC-AGCM. This is the main documentation for the new version of the atmospheric model. Therefore I would expect to find here basic information for all processes. This should include the numerical techniques used in the dynamics, the transport scheme and the physics. This basic information should be kept concise, so that most of the room can still be devoted to the subsections (a) to (d) for the changes compared to the preceding documented version.**

**Response**: For the completeness of the documentation, we added more detailed descriptions on the model dynamics core, and all the models physics are summarized in Table 2.

**L96: … considered …→… considers …**
**L100: … environment, The mass …→… environment, the mass…**
**L128:… at each model grid …→ …in each model grid cell …?**
**L138: …T_con → T_conv …**

**Response:** Corresponding modifications are now included.

**L144: "… Following the method above, the cloud fraction (C_deep and C_shallow),temperature (T_deep and T_shallow), specific humidity (q_deep and q_shallow) for the deep convective, shallow convective clouds can be then deduced sequentially…." Does the scheme allow the concurrent occurrence of shallow and deep convection in the same atmospheric column, or is only one type of convection allowed at any one time in a single column? If concurrent occurrence is allowed, how is the parametrized computation of deep and shallow convection split, and how is the necessarily sequential diagnostics of C, T and q in the shallow and deep updrafts organized?**

**Response**: We have rewritten this part of the manuscript. In fact, shallow and deep convections can concurrently occur in the same atmospheric column at any time step. The shallow convection follows the deep convection, and it occurs at vertical layers where local instability still remains after the deep convection. In BCC models, the three moisture

processes (i.e. deep convection, then shallow convection, and finally stratiform precipitation) is sequentially executed. That means, the model-box mean T and q are updated immediately after each process.

**L151 and L153: These equations can be numerically unstable in the limit of C_deep+C_shallow!1, because of the division by (1-Cdeep-Cshallow) that is needed to obtain the unknowns T_ambient and q_ambient. Is this a practical problem, or rendered irrelevant by the multiplication factor (1-C_conv) in Eq. 2?**

**Response:** We have added "if $C_{deep} + C_{shallow} > 1$, $C_{deep}$ and $C_{shallow}$ are then scaled to meet the condition $C_{deep} + C_{shallow} = 1.0$, and Cs=0." So we do not need to know the values of T_ambient and q_ambient to derive Cs using Eq. (10).

**L157: : : : RH_abmient : : : ! : : : RH_ambient : : :**
**L164: I cannot find the publication by 'Kristj ÌA¸ansson and Kristiansen [2000]'. Do you mean 'Kristjánsson et al., 2000'? Kristjánsson, J. E., J. M. Edwards, and D. L. Mitchell (2000), Impact of a new scheme for optical properties of ice crystals on climates of two GCMs, J. Geophys. Res., 105(D8), 10063–10079, doi:10.1029/2000JD900015.**
**L202: : : : k = 1.18 _ 106 cmˆ□1 secˆ□1 : : : ! : : : k = 1.18 _ 10ˆ6 cmˆ□1 secˆ□1 : : :**

**Response:** They are corrected now.

**L206: Section 'd. Parameterization of gravity wave drag' This paragraph discusses drag by dissipating gravity waves originating from flow over orography or atmospheric sources. What about drag by blocking effects from unresolved orography? Are such effects, which sometimes are included in gravity wave parameterizations, considered in BCC-AGCM3-MR?**

**Response:** The scheme of gravity wave drag generated from convective sources is that in Beres et al. (2004). The drag by blocking effects is still not involved in present version of BCC-AGCM3-MR.

**L221:... This parameterization scheme of convective gravity waves can improve the model's ability to simulate the stratospheric quasi-biennial oscillation in BCC-AGCM3-MR. … This is a rather general statement. It is clear that non-orographic gravity waves make a significant contribution to the forcing of the QBO, and if the gravity waves are not resolved, then their effect needs to be parameterized for the simulation of the QBO, and tunable parameters can be used to improve the structure of the QBO. Is the CF parameter, which you tune, valid for all latitudes or only for equatorial latitudes, where the QBO exists?**

**Response**: The convective fraction (CF) within a grid cell is an important parameter and is closely related to the deep convection process. It is tuned to obtain the right wave amplitudes. In BCC-AGCM3-MR, it is a constant and does not vary geographically. So it is valid for all

latitudes where convection occurs.

**L277: Is the "simple scheme about the surface albedo, roughness length, turbulent sensible and latent heat fluxes over rice paddies" documented, or is there a manuscript in preparation? If not, and if the scheme is indeed simple, you should include the documentation here.**

**Response**: A new manuscript for this regard is indeed under preparation by our team in charge of land surface processes.

**L348: …The preindustrial climate state of BCC-CSM2-MR is preceded by a more than 500 years piControl simulation following the requirement of CMIP6. …Which were the goals of the spin-up simulation for the piControl experiment? Which were the criterions for declaring the spin-up phase completed? It would be interesting to learn about these criterions.**

**Response:** In the revised manuscript, we added some details about how the spinup was effectively accomplished. For this issue, we just followed the recommendations from CMIP project. Basically we check the steadiness of some globally-integrated quantities. We also added Fig.2 in the revised manuscript, showing energy balance at top of the atmosphere.and surface air temperature over the globe in the piControl simulation.

**L.353: : : : the up-limit of the atmosphere : : : ! : : : the top of the model atmosphere : : :**
**Response**: Modified.

**L.362: …It means that the whole earth system in our models is very close to energy equilibrium. … For a transient period it is a bit difficult to judge from the similarity between TOA radiation fluxes of the model and the observations whether the model is generally in a "good" equilibrium. How is the energy balance for the preindustrial control experiment? Here we know that the net energy flux at TOA should be zero except for fluctuations related to the internal variability of the coupled system. If the model system has energy leaks, as many climate models have, we should see this clearly in the stabilized piControl simulation. Such a leakage would have to be considered in the comparison of the transient TOA radiation fluxes of the model and the observations. My suggestion is that you discuss the net energy flux at TOA and the surface and maybe other quantities of interest of the piControl simulation before starting the discussion of the historical simulation. This could for instance be embedded in a new section that explains the tuning goals of the piControl experiment.**

**Response:** Yes, we agree with the referee's reasoning. It is a bit difficult to judge from the similarity between TOA radiation fluxes of the model and the observations. We have modified the description. In addition, following referee's suggestion, we have added Figure 2 (in the revised manuscript) in Section 3 to show the time series of annual mean of net energy flux at top of the atmosphere and the global sea surface temperature from 600 years piControl

simulation. It means that the whole system in BCC-CSM2-MR nearly reaches its equilibrium after 600 years piControl simulation.

**L372: : : : These biases are reduced in BCC-CSM2-MR. : : : Which of the model changes discussed earlier cause the strong (and useful) changes in the tropical SW and LW cloud radiative forcing between the old and new model?**

**Response:** Modified. In low latitudes between 30 ℃S and 30 ℃N, BCC-CSM1.1m shows excessive cloud radiative forcing for both shortwave and longwave radiations. These biases are reduced in BCC-CSM2-MR and may be attributed to the new algorithm in diagnosing cloud fraction especially convective cloud amount.

**L379: : : : Biases of annual mean surface air temperature (at 2 meters) : : : Figure 2 shows the spatial patterns of the T2m bias. But first of all I am wondering how the transient global mean temperature is evolving from the stabilized pre-industrial mean temperature representative for 1850 to the present day. Please discuss first the global mean evolution before describing the pattern of the T2m bias near the end of the historical experiment. Further, it would be interesting to read your opinion on the contribution of the model changes to the observed differences between the models. Can you attribute the disappearance of the cold bias in the southern oceans in the new model compared to the old model to the changes in the model for turbulent fluxes over sea ice? Are specific changes of the land model important for the increased cold bias in east Asia and Siberia in the new model compared to the old model? For the land surface biases it would be valuable to know if these patterns are already present in AMIP simulations, where effects of oceanic biases are excluded.**

**Response:**

(1) Following referee's suggestion, we advanced two sections (old Section 4.4 and Section 4.5) to the position just after Section 4.1. They become now Section 4.2 and Section 4.3. The former presents the transient global mean temperature evolving from 1850 to the present day, and the latter (new Section 4.3) presents climate sensitivity to CO2 increasing.

(2) As shown in Figure 2 (in the initial manuscript, and renumbered to Fig.5 in the revised manuscript), the disappearance of the cold bias in the Southern Oceans in BCC-CSM2-MR (compared to BCC-CSM1.1m) is quite certainly attributable to the new scheme of cloud fraction parameterization implemented in BCC-CSM2-MR, which largely improves the low-level clouds simulation between 40 ℃S to 60 ℃S over the Southern Ocean (not shown).

(3) Biases over land surface in the two coupled models are similar to each other. They are furthermore already present in AMIP. So biases over land surface (at least partly) come from the land surface model.

**L386: annual mean precipitation What is the global mean precipitation in both models? Do you have any thoughts about the contribution of the changes in the deep convection scheme to the strong wet bias in the Maritime Continent?**

**Response**: The global mean precipitation rates in BCC-CSM1.1m and BCC-CSM2-MR are 2.87 mm/day and 2.94 mm/day, respectively. A precipitation rate of 2.68 mm/day is the 1986-2005 mean observed precipitation from Global Precipitation Climatology Project (Adler et al., 2003). The excessive rainfalls in the Maritime Continent seem amplified in BCC-CSM2-MR, which is attributed to abundant stratiform precipitation which accounts 39% of total precipitation in BCC-CSM2-MR. That percentage was 35% in BCC-CSM1.1m.

**L. 393: … The evaluation is done against climatology of ERA-Interim … NCEP dataset … From the text and the figure caption it seems rather that only NCEP is used and not ERA-Interim. Can you please clarify this?**

**Response**：It was a mistake. In fact, ERA-Interim is used as a reference state instead of NCEP.

**L421:…Given a much higher vertical resolution and an advanced parameterization of the gravity wave drag … Despite the more complete parameterization of gravity wave drag – now including gravity waves from atmospheric sources – the zonal mean zonal wind biases in the high latitudes of the stratosphere have increased near 10 hPa, where one would expect the main benefit from gravity wave parameterizations. Can you explain why there is no benefit from the improved GWD parameterization on the structure of the polar night jets? Did you attempt to tune the gravity wave drag to reduce errors in the stratospheric extratropical zonal circulation?**

**Response:** We don't know the exact cause for the zonal wind biases in the stratosphere of high latitudes in BCC-CSM2-MR. Maybe the lack of gravity wave drag generated by atmospheric blocking is the explanation. We expect to reduce the bias in next version by adding this process.

**L427: … In Figure 6(b), the BCC-CSM2-MR simulations present a clear quasi-biennial oscillation of the zonal winds as observed. …The downward propagation … does not penetrate to sufficiently low altitudes. … Though the vertical resolution is increased, it is still too low to expect a QBO simulation down to at least 70 hPa, because the forcing from resolved waves cannot be adequately resolved. Therefore it seems like the QBO occurring in the new model must be dependent entirely or nearly entirely on the Beres parameterization. Has this scheme been tuned to obtain the QBO in the new model?**

**Response:** Yes, we agree with the referee's arguments. The number of layers (46) in our model is certainly too low to resolve adequately vertically-propagated waves. But we have not tuned the Beres scheme that seems to work well in our new model. This issue deserves further studies in the future.

**L470: : : : The most remarkable improvements of BCC-CSM2-MR appear in the boreal warm seasons, : : : To which model improvement do you attribute the strong improvement of SIE or SIC?**

**Response:** It is hard to say. Those improvements may be partly contributed by many aspects of new model physics schemes such as turbulent flux over sea ice and ocean surfaces, cloud fraction, or atmospheric circulation improvement at high latitudes.

**L495: : : : Our CMIP6 model can capture this warming hiatus. : : : The word "capture" suggests that the hiatus is a predictable climate feature that a coupled climate simulation can be expected to reproduce if the forcing is realistic and the model is "correct". Is this what you want to express? Maybe it is better to write for instance: "The historical simulation of the CMIP6 model shows a hiatus towards the end of the simulation that resembles the observed one." Do you have other ensemble members for the historical CMIP6 simulation, and if so do all members reproduce the hiatus of 1998-2013? The figure shows also that the CMIP5 simulation is significantly colder in the early decades than observations or the CMIP6 simulation. Later on, however, both simulations evolve by and large in a similar way. Can this be explained by the external forcing (volcanic aerosols?)? Do you have any insight that you can share?**

**Response:** To address this comment, we need to point out three elements. (1) The phrase concerning the simulated warming hiatus has been changed in the revised manuscript as suggested. (2) As many CMIP diagnostic papers, we also used only one member in our manuscript. That member shows hiatus. Recently, two additional members of the historical simulation are also available. As shown in new Figure 4, two members show hiatus towards the end of the simulation. (3) Both BCC models seem too sensitive to volcanic aerosols. But we do not fully understand the behaviors of global mean temperature curves.

**L509: …Observation-based NSIDC data are also plotted when available. … The caption for Fig. 11 reads: ": : : observations-based Hadley Centre Sea Ice and Sea Surface Temperature data set (Rayner et al., 2003)." Please clarify.**

**Response:** Modified. In Figure 11 (in the initial manuscript, and renumbered to Fig.14 in the revised manuscript), the observed sea-ice extent are derived from Hadley Centre Sea Ice and Sea Surface Temperature data set. In Figure 8 (now renumbered to Fig.15), the observed seasonal cycles of sea-ice extent in (a) and (b) are based on the National Snow and Ice Data Center (NSIDC; Fetterer et al., 2002) data sets. In order to keep consistency, the NSIDC data in Figure 8 (now renumbered to Fig.15) is replaced by Hadley data.

**L516: 4.5 Climate sensitivity to CO2 increasing Figure 12 following Gregory (2012) not only provides estimates for the ECS, but primarily provides information on the climate feedback. Comparing both models, the ECS is similar, but the feedback parameter is substantially different: BCC-CSM3-MR: ca. -1 W/m2/K; BCC-CSM1.1m: ca. -1.3 W/m2/K Thus the result that both ECS values are very similar results only because the initial 4xCO2 forcing is quite different: BCC-CSM3-MR: ca. 6 W/m2; BCC-CSM1.1m: ca. 7.5 W/m2/K Can you please comment on the origin of the large difference in the initial forcing?**

Response: Yes, that's an interesting point. We added a paragraph in the revised manuscript concerning the 4xCO2 initial forcing, feedbacks and ECS. Due to changes of atmospheric profiles (temperature, water vapor and cloud), it is possible to have different forcing for a quadruple CO2, and even the radiative transfer is unchanged. Feedbacks operate certainly in different ways in the two models. What is interesting is that the final ECS converges between the two models.

**L529: : : : abruptCO2 : : : ! : : : abrupt4xCO2 : : : ?**
Response: Modified.

**Response to Anonymous Referee #2**

**This is a description paper of BCC-CSM2-MR. The upgraded schemes are well described, while evaluations for internal variability and long-term trends are insufficient. Authors emphasized improvements in several aspects. Some of them (e.g., representation of QBO) are remarkable improvements but some others are not very convincing. Major revisions and some additional analyses are required as follows:**

**Major comments:**
**The paper lacks the information of ensemble size of each historical runs. The following two comments are related to this issue:**

**1.1 Is the global warming trend of CMIP6 model shown in Fig. 10 the ensemble-mean value? What is the gray shading? Maximums/minimums of CMIP5? If the ensemble size of CMIP6 is only one member, you cannot deny the possibility that the simulated slowdown after 1998 happened by chance due to natural variability. On the other hand, if it is ensemble-mean value, then the slowdown after 1998 implies it is the result of external forcing. In the latter case, you need to discuss whether the difference in the trends between CMIP5 and CMIP6 is due to the difference in external forcing or the model update.**

**Response：**
The mentioned curves (in old Fig. 10 or new Fig. 4) are from a single realization for both BCC models (CMIP5 and CMIP6). After the initial submission of the manuscript, two other members are now available for our CMIP6 exercises, which are added in the new Fig. 4. Gray shaded area shows the spread calculated from 31 CMIP5 models. The caption in Fig. 10 of the initial manuscript was not clear, and is now modified in the new manuscript. Concerning the global warming hiatus or slowdown after 1998 in old Figure 10 (or new Fig.4, it is the overlay of internal variability and long-term trends. We need to explore it further in the future. Among the three members, two show some features of hiatus.

**1.2 Is the improvement of MJO shown in Fig. 7 robust? A correlation coefficient depends on a sample size. Are the sample sizes (the total numbers of years) you used for the analyses of the observation, BCC-CLM1.1m, and BCC-CLM2-MR comparable? If the improvement is true, what do you think is a factor improving the representation of MJO? New convection scheme?**

**Response:** Yes, MJO activities largely depend on period and time length of analysis. But we believe that our analysis in Figure 7 is robust and consistent: all data for observation, BCC-CSM1.1m, and BCC-CSM2-MR are from the same period from 1997 to 2005. We believe that the improvement of MJO simulation in BCC-CSM2-MR is true and can be possibly attributed to deep convection scheme (Table 2). Further investigations are underway.

**2 It seems that the results in Fig. 8 and Fig. 11 are inconsistent. Is it due to the difference**

**between the reference datasets (NSIDC, ECMWF forecasts, and Hadley Centre Sea Ice)? Please add some explanation to figure out it and the reason why you used those datasets.**

**Response:**
Figure 11a and 11b (in the old version of manuscript) shows seasonal cycle of sea-ice extent climatology, in which the observation data is derived by National Snow and Ice Data Center (NSIDC; Fetterer et al., 2002) and are directly downloaded from https://svn-ccsm-models.cgd.ucar.edu/tools/proc_ice/trunk/ice_diag/data/SSMI.ice_extent.1981-2005.monthly.regional.txt. Figure 11c and 11d (in the old version of manuscript) shows seasonal cycle of sea-ice thickness averaged for the Northern Hemisphere and the Southern Hemisphere, which is computed based on 1980-2005 global monthly 1/4 °x1/4 °gridded dataset based on European Center for Medium-Range Weather Forecast (Tietsche, et al., 2014).

Figure 8 (in the initial manuscript) presents long term change of sea-ice extent from 1851 to 2012, the observed data are computed based on global monthly 1 °x1 ° gridded dataset of Hadley Centre Sea Ice and Sea Surface Temperature (Rayner et al., 2003).

The observed sea-ice extent in Figs. 11 and 8 (in the initial manuscript) doesn't come from a same source. NSIDC data are mainly derived from satellite observations, so with a higher quality. But they cover a too-short period. This explains why Fig. 8 in the initial manuscript the long-lasting Hadley Centre Sea Ice and Sea Surface Temperature data set. For the sake of consistency, we decided to use only Hadley center data throughout the manuscript.

**3 Section 4.2: Please discuss the SST cold bias in the equatorial Pacific and the double ITCZ problem. Evaluations for the subsurface ocean (temperature, zonal currents) are also required.**

**Response:**
We added two more figures to discuss the SST cold bias and the interannual variations of NINO3.4 SST in the equatorial Pacific. As length of the paper is limited and there are already 20 figures, the subsurface ocean (temperature, zonal currents) will be explored in the future.

**4 Section 4.6: There is a large seasonal cycle in the East Asian climate. Analyses should be done for each season, especially for JJA and DJF.**
**Response:** We added a further figure to discuss the DJF and JJA precipitation in East Asia.

**5 Comparison of ENSO representation (NINO3.4 time series, amplitude, spatial pattern etc.) is necessary to evaluate the model performance.**
**Response**: We added a figure to show behaviors of Nino3.4 time series. The detail evaluation for ENSO representation will be analyzed in other papers.

**Minor issues:**
**6 L19: models -> model's**

**7 L27-28 "Compared to BCC CMIP5 models, BCC CMIP6 models show: : :": The expression "models" is inappropriate. This paper compared only one model for each (BCC-CSM1.1m for CMIP5 and BCC-CSM2-MR for CMIP6).**
**8 L41: More -> more**
**9 L53: The full name of CMIP5 and Taylor et al. (2012) should appear at L42.**
**10 L59: Please comment on Section 5 and 6.**
**11 L64: Please add the full name for NCAR.**
**12 L64: Coupler -> coupler**
**Response:** 6-12, all done.

**13 L65-66: Are tuning parameters also the exactly same between the two models?**
**Response:** Some physical schemes in the two models are not the same. Tuning parameters are not exactly the same, neither.

**14 L79: Please add the level of the top layer.**
**Response:** Added as suggested. The tops of atmosphere in BCC-CSM1.1m and BCC-CSM2-MR are at 2.917hPa and 1.459 hPa, repsecctively.

**15 L240: What is the CEVSA model?**
**Response:**CEVSA model is the carbon exchange between vegetation, soil and the atmosphere (CEVSA) model

**16 L243: Table 2 -> Table 3**
**Response:** Modified.

**17 L362: 2014 -> 2005? The end of the CMIP5 historical run is 2005.**
**Response:** Modified. In Table 4, and Fig.1 (renumbered to Fig.3 in the revised manuscript), model results are for the period 1986–2005, while the available CERES-EBAF data are for 2003–2014.

**18 L371 "1986-": "1985-" in the caption of Fig. 1**
**Response:** Modified.

**19 L374-376: In the mid latitude, discrepancies in the two observations are also large. You cannot discuss the difference between the two models.**
**Response:** Modified as suggested.

**20 L396: Precipitation data diagnosed in reanalysis is not necessarily correct. You had better use the observation-based dataset.**
**Response:** Modified as suggested.

**21 L406: Figure 4s -> Figure 4**
**Response:** Modified.

**22 L409: Were there any reason you used the two different reanalysis datasets (NCEP and ERA-interim) for each analysis?**
**Response:** Modified. All the reanalysis data used to draw figures are now replaced by ERA-interm.

**23 L437 "forcing is less adequate": What forcing?**
**Response:** "forcing" denotes gravity wave forcing. Modified to "The amplitudes of the QBO cycles in the simulation are weaker than in the reanalysis, which is possibly due to inadequate gravity wave forcing to drive the QBO."

**24 L452: improvementcompared -> improvement compared**
**Response:** Modified.

**25 L478-481: Is the lower and deeper NADW better? Please show the observation based values.**
**Response:** Modified. The observation-based value is 25 Sv in Talley et al. (2013).

**26 L486 "from 60S to 60N": Why did not you use the average from 90S to 90N?**
**Response:** Only the area from 60°S to 60°N is averaged in Fig. 10 (renumbered to Fig.4 in the revised manuscript). This is mainly motivated by the consideration that HadCRUT4 dataset had very few observations in polar regions in earlier 20$^{th}$ century.

**27 L491, L500: HadCRU -> HadCRUT4**
**Response:** Modified.

**28 L503: Figure 2c -> Figure 10?**
**Response:** Modified.

**29 L529: abruptCO2 -> abrupt CO2**
**Response:** Modified.

**30 L535 "the TCR of the new version model BCC-CSM2-MR is lower than BCCCSM1.1m,": lower -> higher? It is inconsistent with L527-528.**
**Response:** The TCR of the new version model BCC-CSM2-MR is lower than BCC-CSM1.1m, but the ECS of BCC-CSM2-MR is slightly higher than BCC-CSM1.1m.

**31 L566-567: Are there any impact of the upgraded land surface scheme on the improvement of the rainfall diurnal cycle?**
**Response:** We didn't explore this issue, but we think the upgraded land surface scheme has minor role for the improvement of the rainfall diurnal cycle.

**32 L616-620: Please see 31.**
**Response:** Modified.

**33 Table 3 "(Guenther et al., 2012)": Please check the font.**
**Response:** Modified.

**34 Table 4: What is the value of the net energy at TOA for OBS? 0.81?**
**Response:** The net energy at TOA is 0.81 W $m^{-2}$ for CERES-EBAF and 5.73 W $m^{-2}$ for CERES data.

**35 Table 4, Notes, "1981-2014": 1981-2005 for BCC-CSM1.1m? Why are the periods slightly different among the figures or tables (1985-2005 for Fig. 1, 1986-2005 for Fig. 2-3 and 5, 1980-2005 for Fig. 4, 8-9, 13)?**
**Response:** Yes, that's done. We apologize for the inconsistency. However, In Table 4 and Fig. 1 (renumbered to Fig.3 in the revised manuscript), model data are the mean from 1986 to 2005, while observation is only available for 2003–2014.

**36 Figure 7 d-f: Please show the range of longitude used for the average to obtain the latitude-time section.**
**Response:** Modified.

**37 Figure 14: The result of BCC-CSM1.1m (BCC-CSM2-MR) should be in the bottom (middle) as same as in the other figures.**
**Response:** Yes, that's done. We appologize for the inconsistency.

# The Beijing Climate Center Climate System Model (BCC-CSM): Main Progress from CMIP5 to CMIP6

**Tongwen Wu[1*], Yixiong Lu[1], Yongjie Fang[1], Xiaoge Xin[1], Laurent Li[1,2], Weiping Li[1], Weihua Jie[1], Jie Zhang[1], Yiming Liu[1], Li Zhang[1], Fang Zhang[1], Yanwu Zhang[1], Fanghua Wu[1], Jianglong Li[1], Min Chu[1], Zaizhi Wang[1], Xueli Shi[1], Xiangwen Liu[1], Min Wei[3], Anning Huang[4], Yaocun Zhang[4], Xiaohong Liu[1,5]**

[1]Beijing Climate Center, China Meteorological Administration, Beijing, China
[2]Laboratoire de Météorologie Dynamique, IPSL, CNRS, Sorbonne Université, Ecole Normale Supérieure, Ecole Polytechnique, Paris, France
[3]National Meteorological Information Center, China Meteorological Administration, Beijing, China
[4]Nanjing University, Nanjing, China
[5]University of Wyoming, Laramie, WY, United States

*Correspondence to:* Tongwen Wu (twwu@cma.gov.cn)

**Abstract**. Main progresses of Beijing Climate Center (BCC) climate system model from the phase five of the Coupled Model Intercomparison Project (CMIP5) to its phase six (CMIP6) are presented, in terms of physical parameterizations and model's performance. BCC-CSM1.1 and BCC-CSM1.1m are the two models involved in CMIP5, and BCC-CSM2-MR, BCC-CSM2-HR, and BCC-ESM1.0 are the three models configured for CMIP6. Historical simulations from 1851 to 2014 from BCC-CSM2-MR (CMIP6) and from 1851 to 2005 from BCC-CSM1.1m (CMIP5) are used for models assessment. The evaluation matrices include (a) energy budget at top of the atmosphere, (b) surface air temperature, precipitation, and atmospheric circulation for global and East Asia regions, (c) sea surface temperature (SST) in tropical Pacific, (dc) sea ice extent and thickness and Atlantic Meridional Overturning Circulation (AMOC), and (ed) climate variations at different time scales such as global warming trend

in the 20th century, stratospheric quasi-biennial oscillation (QBO), Madden-Julian Oscillation (MJO) and diurnal cycle of precipitation. Compared to BCC-CSM1.1m ~~-CMIP5 models~~, BCC-CSM2-MR ~~CMIP6 models~~ shows significant improvements in many aspects including: tropospheric air temperature and circulation at global and regional scale in East Asia, climate variability at different time scales such as QBO, MJO, diurnal cycle of precipitation, interannual variations of ~~-~~SST in the equatorial Pacific, and long-term trend of surface air temperature.

## 1. Introduction

Changes of global climate and environment are main challenges that human societies are facing for sustainable developments. Climate and environment changes are often the consequence of combined effects of anthropogenic influences and complex interactions among the atmosphere, hydrosphere, lithosphere, cryosphere and biosphere of the Earth system. To better understand behaviors of the earth climate, and to predict its future evolution, appropriate new concepts and relevant methodologies should be proposed and developed. Climate system models are effective tools to simulate the interactions and feedbacks in an objective manner, and to explore their impacts on climate and climate change. The Coupled Model Intercomparison Project (CMIP) organized under the auspices of the World Climate Research Programme's (WCRP) Working Group on Coupled Modelling (WGCM) started twenty years ago as a comparison of a handful of early global coupled climate models (Meehl et al., 1997). ~~Many climate models in the world have been developed since the IPCC AR4,~~ More than 30 models participated in the phase five of CMIP~~5~~ ~~project~~(CMIP5, Taylor et al., 2012) and created an unprecedented dynamics in the scientific community to generate climate information and make them available for scientific researches. Many of these models were then extended into Earth System models by including the representation of biogeochemical cycles. BCC effectively contributed to CMIP5 by running most of the mandatory and optional simulations.

The first generation of Beijing Climate Center ocean-atmosphere Coupled Model BCC-CM1.0 was developed from 1995 to 2004 (e.g. Ding et al., 2002). It was mainly used for seasonal climate prediction. Since 2005, BCC initiated the development of a new fully-coupled climate modelling platform (Wu et al., 2010, 2013, 2014). In 2012, two versions of the BCC model were released: BCC-CSM1.1 with a

coarse horizontal resolution T42 (approximately 280 km) and BCC-CSM1.1m with a medium horizontal resolution T106 (approximately 110 km). It was a fully-coupled model with ocean, land surface, atmosphere, and sea-ice components (Wu et al., 2008; Wu, 2012; Xin et al., 2013). Both versions were extensively used for CMIP5~~the phase five of the Coupled Model Intercomparison Project (CMIP5, Taylor et al., 2012)~~. At the end of 2017, the second generation of the BCC model was released to run different simulations proposed by the phase six of ~~the Coupled Model Intercomparison Project~~ CMIP (CMIP6, Eyring et al., 2016). The purpose of this paper is to document the main efforts and progress achieved in BCC for its climate model transition from CMIP5 to CMIP6. We show improvements in both model resolution and its physics. A relevant description on model transition, and experiment design are~~is~~ shown in Sections 2 and 3. A comparison of models performance is presented in Section 4. Conclusions and discussion are summaried in Section 5. Information about code and data availability is shown in Section 6.

## 2. Transition of the BCC climate system model from CMIP5 to CMIP6

Table 1 shows a summary of different BCC models or versions used for CMIP5 and CMIP6. All of them are fully-coupled global climate models with four components, atmosphere, ocean, land surface and sea-ice, interacting with each other. They are physically coupled through fluxes of momentum, energy, water at their interfaces. The coupling was realized with the ~~the NCAR~~ flux c~~C~~oupler version 5 developed by the National Center for Atmosphere Research (NCAR). BCC-CSM1.1 and BCC-CSM1.1m are our~~the~~ two models involved in CMIP5. They differ only by their horizontal resolutions. As shown in Table 1, BCC-CSM2-MR, BCC-CSM2-HR, and BCC-ESM1.0 are the three models developed for CMIP6.

BCC-ESM1.0 is our Earth System configuration. It is a global fully-coupled climate-chemistry-carbon model, and intended to conduct simulations for the Aerosol Chemistry Model Intercomparison Project (AerChemMIP, Collins et al., 2017) and the Coupled Climate–Carbon Cycle Model Intercomparison Project (C4MIP, Jones et al., 2016), both endorsed by CMIP6. Its performance will be ~~is~~ presented in a separated paper ~~(Wu et al., to be submitted)~~. BCC-CSM2-HR~~, also presented separately,~~ is our high-resolution configuration prepared for conducting simulations of the High

Resolution Model Intercomparison Project (HighResMIP v1.0, Haarsma et al., 2016). It has 56 layers in the vertical, 0.092 hPa for the top of model. Its performance will also be presented separately.

In this paper, we focus on BCC-CSM1.1m and BCC-CSM2-MR. The two models ~~which~~ are representative of our climate modelling efforts in CMIP5 and CMIP6 respectively. They have the same horizontal resolution (T106, about 110×110 km in the atmosphere and 30×30 km in the tropical ocean), ensuring a fair comparison. But they have different vertical resolutions in the atmosphere (Table 1), which are 26 layers with its top at 2.917 hPa in BCC-CSM1.1m and 46 layers with its top at 1.459 hPa in BCC-CSM2-MR (Figure 1). The present version of BCC-CSM2-MR takes 50% more computing time than BCC-CSM1.1m for the same amount of parallel computing processors.

**2.1 Atmospheric component BCC-AGCM**

The atmospheric component of BCC-CSM1.1m is BCC-AGCM2.2 (second generation). It is detailed in a series of publications (Wu et al., 2008, 2010; Wu, 2012; Wu et al., 2013). BCC-AGCM3-MR is its updated version (third generation), used as the atmosphere component in BCC-CSM2-MR. ~~Table 2 summarizes the main differences of model physics of our atmospheric GCMs between BCC-AGCM2.2 and BCC-AGCM3-MR.~~ The dynamic core in the two models is identical and uses the spectral framework described in Wu et al. (2008), in which a reference stratified atmospheric temperature and a reference surface pressure are introduced into the governing equations to improve pressure gradient force and gradients of surface pressure and temperature, the prognostic variables for temperature and surface pressure are separately replaced by their perturbations from their references. Explicit time difference scheme is applied to vorticity equation, and semi-implicit time difference scheme for divergence, temperature, and surface pressure equations. Semi-Lagrangian tracer transport scheme is used for water vapor, liquid cloud water and ice cloud water. ~~Table 2 summarizes the m~~Main differences of model physics used in the two models ~~of our atmospheric GCMs between~~ (BCC-AGCM2.2 and BCC-AGCM3-MR) are summarized in Table 2 and details in the. ~~Some details are as~~ followings:

***a. Deep convection ~~parameterization~~***

Our second-generation atmospheric model, BCC-AGCM2.2, operates with a parameterization scheme of deep cumulus convection developed by Wu (2012). Main characteristics can be summarized

as follows:

(1) Deep convection is initiated at the level of maximum moist static energy above the boundary layer. It is triggered when there is positive convective available potential energy (CAPE) and if the relative humidity of the air at the lifting level of convective cloud is greater than 75%;

(2) A bulk cloud model taking into account processes of entrainment/detrainment is used to calculate the convective updraft with consideration of budgets for mass, dry static energy, moisture, cloud liquid water, and momentum. The scheme ~~is~~ also consider~~s~~ed the lateral entrainment of the environmental air into the unstable ascending parcel before it rises to the lifting condensation level. The entrainment/detrainment amount for the updraft cloud parcel is determined according to the increase/decrease of updraft parcel mass with altitude. Based on a total energy conservation equation of the whole adiabatic system involving the updraft cloud parcel and the environment, t~~T~~he mass change for the adiabatic ascent of the cloud parcel with altitude is derived;

(3) The convective downdraft is assumed to be saturated and originated from the level of minimum environmental saturated equivalent potential temperature within the updraft cloud;

(4) The closure scheme determining the mass flux at the base of convective cloud is that suggested by Zhang (2002). It assumes that the increase/decrease of CAPE due to changes of the thermodynamic states in the free troposphere resulting from convection approximately balances the decrease/increase resulting from large-scale processes.

A modified version of Wu (2012) is used in BCC-AGCM3-MR for deep convection parameterization. The convection is triggered only when the boundary layer is unstable or there exists updraft velocity in the environment at the lifting level of convective cloud, and simultaneously there is positive CAPE. This modification is aimed to connect the deep convection to the instability of the boundary layer. The lifting condensation level is set to above the nominal level of non-divergence (600 hPa) in BCC-AGCM2.2 and lowered to the level of 650 hPa in BCC-AGCM3-MR. These modifications in the deep convection scheme are found to improve the simulation of diurnal cycle of precipitation and Madden-Julian Oscillation (MJO).

***b. Shallow convection***

Shallow convection is parameterized with a local convective transport scheme (Hack, 1994). It is

used to remove any local instability that may remain after the deep convection scheme. This Hack convection scheme is largely-used one to typically represent shallow subtropical convection and midlevel convection that do not originate from the boundary layer.

***c. Cloud macrophysics***

Cloud macrophysics comprises physical processes to compute cloud fractions in each layer, horizontal and vertical overlapping of clouds, and conversion rates of water vapor into cloud condensates.

~~***b. Cloud fraction***~~

In BCC-AGCM2.2, cloud fraction and the associated cloud macrophysics follow what designed in NCAR Community Atmosphere Model version 3 (CAM3, Collins et al., 2004). T~~t~~he total cloud cover ($C_{tot}$) within each model grid is set as the maximum value of three cloud covers: low-level marine stratus ($C_{mst}$), convective cloud ($C_{conv}$), and stratus cloud ($C_s$),

$$C_{tot} = \max\left(C_{conv}, C_{mst}, C_s\right) \quad (1)$$

As in CAM3, the marine stratocumulus cloud is diagnosed with an empirical relationship between the cloud fraction and the boundary layer stratification which is evaluated with atmospheric variables at surface and 700mb (Klein and Hartmann, ~~[~~1993~~]~~). The convective cloud fraction uses a functional form of Xu and Krueger (~~[~~1991~~]~~ ) relating the cloud cover to updraft mass flux from the deep and shallow convection schemes. The stratus cloud fraction is diagnosed on the basis of relative humidity which varies with pressure.

A new cloud scheme is developed and used in BCC-AGCM3-MR. It consists of calculating convective cloud and the total cloud cover in a different way from BCC-AGCM2.2. The total cloud fraction in ~~at~~ each model grid cell is given as

$$C_{tot} = C_{conv} + \left(1 - C_{conv}\right) \cdot \max\left(C_{mst}, C_s\right) \quad (2)$$

And the convective cloud $C_{conv}$ is assumed to be the sum of shallow ($C_{shallow}$) and deep ($C_{deep}$) convective cloud fractions:

$$C_{conv} = C_{shallow} + C_{deep} \quad (3)$$

$C_{shallow}$ and $C_{deep}$ are non-overlapped with each other and diagnosed following the relationships,

$$C_{conv} q^*(T_c) + (1 - C_{conv})\bar{q} = \bar{q}_{conv} \quad (4)$$

$$C_{conv} T_c + (1 - C_{conv})\bar{T} = \bar{T}_{conv} \quad (5)$$

and

$$q^*(T_c) = q^*(\bar{T}) + \frac{\partial q^*(\bar{T})}{\partial \bar{T}}(T_c - \bar{T}) \quad (6)$$

where $\bar{q}$ and $\bar{T}$, $\bar{q}_{conv}$ and $\bar{T}_{conv}$ denote the model grid box-averaged water vapor mixing ratio and temperature in the 'environment' before and after convection activity, respectively. $T_c$ and $q^*(T_c)$ are the temperature inside the convective cloud plume and its saturated water vapor mixing ratio. Here, we assume that the shallow and deep convection can concurrently occur in the same atmospheric column at any time step. That is, the shallow convection scheme follows the deep convection and occurs at vertical layers where local instability still remains after deep convection.

If no supersaturation exists in clouds, we can obtain from Eqs. (4) and (5)

$$C_{conv} = \frac{(\bar{q}_{conv} - \bar{q}) - \frac{\partial q^*(\bar{T})}{\partial \bar{T}}(\bar{T}_{conv} - \bar{T})}{q^*(\bar{T}) - \bar{q}} \quad (7)$$

The temperature $T_c$ and the specific humidity $q_c = q^*(T_c)$ of the cloud plume can be firstly derived from Eqs. (5) and (6). Following the method above, the cloud fraction ($C_{deep}$ and $C_{shallow}$), temperature ($T_{deep}$ and $T_{shallow}$), specific humidity ($q_{deep}$ and $q_{shallow}$) for the deep convective, shallow convective clouds can be then deduced sequentially.

After the three moisture processes (i.e. deep convection, then shallow convection, and finally stratiform precipitation) are finished, and the mean temperature ($\bar{T}_{box}$) and specific humidity ($\bar{q}_{box}$) of the whole model-grid box are then updated. Ambient temperature ($\bar{T}_{ambient}$) and specific humidity ($\bar{q}_{ambient}$) outside the convective clouds can be finally estimated using the following Eqs.,

$$\bar{q}_{box} = \bar{q}_{ambient} \cdot (1 - C_{deep} - C_{shallow}) + q_{deep} \cdot C_{deep} + q_{shallow} \cdot C_{shallow}, \quad (8)$$

and

$$\overline{T}_{box} = \overline{T}_{ambient} \cdot \left(1 - C_{deep} - C_{shallow}\right) + T_{deep} \cdot C_{deep} + T_{shallow} \cdot C_{shallow} . \quad (9)$$

Finally, the stratus cloud fraction $C_S$ is diagnosed on the basis of the relative humidity ($RH_{ambient}$) of the ambient,

$$C_s = \left( \frac{RH_{ambient} - RH_{\min}}{1 - RH_{\min}} \right)^2 \quad (10)$$

where $RH_{min}$ is a threshold of relative humidity and $RH_{ambient}$ is derived with $\overline{T}_{ambient}$ and $\bar{q}_{ambient}$. If $C_{deep} + C_{shallow} > 1$ in Eqs. (8) and (9), $C_{deep}$ and $C_{shallow}$ are scaled to meet the condition $C_{deep} + C_{shallow} = 1.0$, and then $C_s = 0$. At that condition, we do not calculate $\overline{T}_{ambient}$ and $\bar{q}_{ambient}$ from Eqs. (8) and (9).

***d. Cloud microphysics***

In BCC-AGCM2.2 and BCC-AGCM3-MR, the essential part of the stratiform cloud microphysics remains the same and follows the framework of non-convective cloud processes in CAM 3.0 (Collins et al., 2004) that is the scheme proposed by Rasch and Kristj ánsson (1998) and modified by Zhang et al. (2003). However there is a noticeable difference of cloud microphysics in the two models concerning the treatments for indirect effects of aerosols through mechanisms of clouds and precipitation.

Indirect effects of aerosols were not included in BCC-AGCM2.2 for CMIP5. That is, the cloud droplets effective radius was not related to aerosols, neither the precipitation efficiency. The cloud droplets effective radius was either prescribed or a simple function of atmospheric temperature. The effective radius for warm clouds was specified to be 14 μm over open ocean and sea ice, and was a function of atmospheric temperature over land. For ice clouds, the effective radius was also a function of temperature following Kristj ánsson et al. (2000).

Aerosol particles influence clouds and the hydrological cycle by their ability to act as cloud condensation nuclei and ice nuclei. This indirect radiative forcing of aerosols is included in the latest version of BCC-AGCM3-MR, with the effective radius of liquid water cloud droplets being related to the cloud droplet number concentration $N_{cdnc}$ ($cm^{-3}$). As proposed by Martin et al. (1994), the volume-weighted mean cloud droplet radius $r_{l,vol}$ can be expressed as

$$r_{l,vol} = \left[ (3LWC) / (4\pi\rho_w N_{cdnc}) \right]^{1/3}, \quad (11)$$

where $\rho_w$ is the liquid water density, LWC is the cloud liquid water content (g $cm^{-3}$). Cloud water and ice contents are prognostic variables in our model with source and sink terms taking into account the cloud microphysics. The effective radius of cloud droplets $r_{el}$ is then estimated as

$$r_{el} = \beta \cdot r_{l,vol} \quad (12)$$

where $\beta$ is a parameter dependent on the droplets spectral shape. There are various methods to parameterize it (e.g. Pontikis and Hicks, 1992; Liu and Daum, 2002). We use the calculation proposed by Peng and Lohmann (2003),

$$\beta = 0.00084 N_{cdnc} + 1.22 \quad (13)$$

In BCC-AGCM3-MR, the liquid cloud droplet number concentration $N_{cdnc}$ ($cm^{-3}$) is a diagnostic variable dependent on aerosols mass. It is explicitly calculated with the empirical function suggested by Boucher and Lohmann (1995) and Quaas et al. (2006) :

$$N_{cdnc} = \exp\left[ 5.1 + 0.41 \ln\left( m_{aero} \right) \right] \quad (14)$$

The total aerosols mass is the sum of four types of aerosol,

$$m_{aero} = m_{SS} + m_{OC} + m_{SO_4} + m_{NH_4NO_2} . \quad (15)$$

Here, $m_{aero}$ ($\mu g.m^{-3}$) is the total mass of all hydrophilic aerosols, i.e., the first bin (0.2 to 0.5 $\mu m$) of sea salt ($m_{SS}$), hydrophilic organic carbon ($m_{OC}$), sulphate ($m_{SO_4}$), and nitrate ($m_{NH_4NO_4}$). Nitrate as a rapidly increasing aerosol species in recent years affects present climate and potentially has large implications on climate change (Xu and Penner, 2012; Li et al., 2014). A dataset of nitrate from NCAR CAM-Chem (Lamarque et al., 2012) is used in our model.

Aerosols also exert impacts on precipitation efficiency (Albrecht, 1989), which is taken into account in the parameterization of non-convective cloud processes. We use the same scheme as in CAM3 (Rasch and Kristj ánsson, 1998; Zhang et al., 2003). There are five processes that convert condensate to precipitate: auto-conversion of liquid water to rain, collection of cloud water by rain, auto-conversion of ice to snow, collection of ice by snow, and collection of liquid by snow. The

auto-conversion of cloud liquid water to rain (PWAUT) is dependent on the cloud droplet number concentration and follows a formula that was originally suggested by Chen and Cotton [1987],

$$PWAUT = C_{l,aut}\, q_l^2 \rho_a / \rho_w \left( \frac{q_l \rho_a}{\rho_w N_{ncdc}} \right)^{1/3} H\left( r_{l,vol} - r_{lc,vol} \right) \tag{16}$$

Where $\hat{q}_l$ is in-cloud liquid water mixing ratio, $\rho_a$ and $\rho_w$ are the local densities of air and water respectively, and

$$C_{l,aut} = 0.55\pi^{1/3} k (3/4)^{4/3} (1.1)^4 . \tag{17}$$

In which k = 1.18 × $10^6$ $cm^{-1}$ $sec^{-1}$ is the Stokes constant. H(x) is the Heaviside step function with the definition,

带格式的：字体颜色：文字 1

$$H(x) = \begin{cases} 0, & x < 0 \\ 1, & x \geq 0 \end{cases} \tag{18}$$

$r_{lc,vol}$ is the critical value of mean volume radius of the liquid cloud droplets $r_{l,vol}$, and set to 15 μ m.

***~~cd~~. ~~Parameterization of Gg~~ravity wave drag***

Gravity waves can be generated by a variety of sources including orography, convection, and geostrophic adjustment in regions of baroclinic instability (Richter et al., 2010). Gravity waves propagate upward from their source regions and break when large amplitudes are attained. This produces a drag on the mean flow. Gravity wave drag plays an important role in explaining the zonal mean flow and thermal structure in the upper atmosphere.

In previous versions of BCC models, the orographic gravity wave drag was parameterized as in McFarlane (1987), but non-orographic sources were not considered. In BCC-AGCM3-MR, the gravity wave drag generated from convective sources is introduced as in Beres et al. (2004), but drag by blocking effects is still not involved. The key point of the Beres' scheme is relating the momentum flux phase speed spectrum to the convective heating properties. In the present version of BCC-AGCM3-MR, the convective gravity wave parameterization is activated only when the deep convective heating depth is greater than 2.5 km.

The uncertainty in the magnitude of momentum flux arises from the horizontal scale of the heating and the convective fraction. The convective fraction (CF) within a grid cell is an important parameter

and can be tuned to obtain right wave amplitudes. It is a constant and ~~do not vary with~~valid for all latitudes where convection is active~~presents~~. Previous studies of Alexander et al. (2004) show that CF can vary from ~0.2% to ~7%–8%. We use 5% in BCC-AGCM3-MR. This parameterization scheme of convective gravity waves can improve the model's ability to simulate the stratospheric quasi-biennial oscillation in BCC-AGCM3-MR.

***f. Radiative transfer***

The radiative transfer parameterization in BCC-AGCM2.2 follows the scheme initially implemented in CAM3 (Collins et al., 2004). Aerosol indirect effects on radiation are not taken into account and cloud droplets effective radius is only function of temperature for cold clouds and prescribed to different values for maritime, polar, and continental cases for warm clouds. In BCC-AGCM3-MR, however, the aerosol indirect effects are fully included and the effective radius of droplets for liquid clouds is calculated by Equation (12) using the liquid cloud droplet number concentration.

***g. Boundary ~~L~~layer turbulence***

BCC-AGCM3-MR basically inherits ~~retains~~ the boundary layer turbulence parameterization used ~~by~~in BCC-AGCM2.2, which is based on the eddy diffusivity approach ~~and BCC-AGCM3-MR, "Non-local" atmospheric boundary layer scheme of ABL parameterization~~ (Holtslag and Boville, 1993). The eddy diffusivity is given by

$$K_c = kw_t z\left(1-\frac{z}{h}\right)^2, \quad (19)$$

where $w_t$ is a turbulent velocity and $h$ is the boundary layer height, which is estimated as

$$h = z_s + \frac{Ri_c\left\{\left[u(h)-u_{SL}\right]^2+\left[v(h)-v_{SL}\right]^2+\beta u_*^2\right\}}{(g/\theta_{SL})\left[\theta_v(h)-\theta_{SL}\right]}, \quad (20)$$

where $z_s$ is the height of the lowest model level, $u$, $v$, and $\theta_v$ are horizontal wind components and virtual potential temperature at height $z$, $u_{SL}$, $v_{SL}$, and $\theta_{SL}$ represent the same variables, but in ~~horizontal wind components and virtual potential temperature in~~ the surface layer.~~,~~ $\beta$ in Eq. (20) is a

带格式的: 字体: (默认) Times New Roman, 小四

带格式的: 缩进: 首行缩进: 0 厘米

域代码已更改

域代码已更改

域代码已更改

带格式的: 缩进: 首行缩进: 0 字符

域代码已更改

域代码已更改

域代码已更改

域代码已更改

域代码已更改

域代码已更改

constant and taken as 100. $u_*$ is the friction velocity, and $g$ is gravitational acceleration. ~~$\beta$ is taken as 100~~

~~, $u_*$ is the friction velocity, and $g$ is gravitational acceleration.~~ The critical Richardson number, ~~,~~ $Ri_c$ in Eq. (20)~~,~~ is a key parameter for calculating the boundary layer height and is set~~assumed~~ to a constant (0.3) for all stable~~ility~~ conditions in BCC-AGCM2.2. In BCC-AGCM3-MR, ~~the values of~~ $Ri_c$ ~~,~~ varies according to conditions of ~~vary with~~ boundary layer stability~~ies~~ to yield more accurate estimates of boundary layer height, and set to ~~based on observational studies:~~ 0.24 for strongly stable conditions, 0.31 for weakly stable conditions, and 0.39 for unstable conditions based on observational studies of ~~(~~Zhang et al.~~,~~ (2014).

域代码已更改

域代码已更改

域代码已更改

域代码已更改

## 2.2 Land component BCC-AVIM

BCC-AVIM, Beijing Climate Center Atmosphere-Vegetation Interaction Model, is a comprehensive land surface scheme developed and maintained in BCC. The version 1 (BCC-AVIM1.0) was used as the land component in BCC-CSM1.1m participating in CMIP5 (Wu et al., 2013). It includes major land surface biophysical and plant physiological processes. Its origin could go back to the Atmosphere-Vegetation Interaction Model (AVIM) (Ji, 1995; Ji et al., 2008) with the necessary framework to include biophysical, physiological, and soil carbon-nitrogen dynamical processes. The biophysical module in BCC-AVIM1.0, with 10 layers for soil and up to five layers for snow, is almost the same as that used in the NCAR Community Land Model version 3 (CLM3) (Oleson et al., 2004). The terrestrial carbon cycle in BCC-AVIM1.0 consists of a series of biochemical and physiological processes modulating photosynthesis and respiration of vegetation. Carbon assimilated by vegetation is parameterized by a seasonally varying allocation of carbohydrate to leaves, stem, and root tissues as a function of the prognostic leaf area index. Litter due to turnover and mortality of vegetation, and carbon dioxide release into atmosphere through the heterogeneous respiration of soil microbes is taken into account in BCC-AVIM1.0. Vegetation litter falls to the ground surface and into the soil is divided into eight idealized terrestrial carbon pools according to the timescale of carbon decomposition of each pool and transfers among different pools, which is similar to that in the carbon exchange between vegetation,

soil and the atmosphere (CEVSA) model ~~CEVSA model~~ (Cao and Woodward, 1998).

BCC-AVIM1.0 has been updated to BCC-AVIM2.0 which serves as the land component of BCC-CSM2-MR participating in CMIP6. As listed in Table 3~~2~~, several improvements have been implemented in BCC-AVIM2.0, such as the inclusion of a variable temperature threshold to determine soil water freezing/thawing rather than fixed at 0°C, a better calculation of snow surface albedo and snow cover fraction, a dynamic phenology for deciduous plant function types, and a four-stream approximation on solar radiation transfer through vegetation canopy. Besides, a simple scheme for surface fluxes over rice paddy is also implemented in BCC-AVIM2.0. These improvements are briefly discussed as follows.

(a) Soil water freezes at the constant temperature 0℃ in BCC-AVIM1.0, but the actual freezing-thawing process is a slowly and continuously changing process. We take into account the fact that the soil water potential remains in equilibrium with the water vapor pressure over pure ice when soil ice is present. Based on the relationships among soil water matrix potential $\psi$ (mm), soil temperature and soil water content, a variable temperature threshold for freeze-thaw dependent on soil liquid water content, soil porosity and saturated soil matrix potential is introduced. The inclusion of this scheme improves the performance of BCC-AVIM2.0 in the simulation about seasonal frozen soil (Xia et al., 2011).

(b) In BCC-AVIM1.0, we took into account the snow aging effect on surface albedo with a simple consideration by using a unified scheme to mimic the snow surface albedo decrease with time. In BCC-AVIM2.0, we assume different reduction rates of snow albedo with actual elapsed time after snowfalls in the accumulating and melting stages of a snow season (Chen et al., 2014). Besides, the variability of sub-grid topography is now taken into account to calculate the snow cover fraction within a model grid cell.

(c) Unlike the empirical plant leaf unfolding and withering dates prescribed in BCC-AVIM1.0, a dynamic determination of leaf unfolding, growth, and withering dates according to the budget of photosynthetic assimilation of carbon similar to the phenology scheme in CTEM (Arora, 2005) was implemented in BCC-AVIM2.0. Leaf loss due to drought and cold stresses in addition to natural turnover are also considered.

(d) The four-stream solar radiation transfer scheme within canopy in BCC-AVIM2.0 is based on the same radiative transfer theory used in atmosphere (Liou, 2004). It adopts the analytic formula of Henyey-Greenstein for the phase function. The vertical distribution of diffuse light within canopy is related to transmisivity and reflectivity of leaves, besides, average leaf angle and direction of incident direct beam radiation influence diffuse light within canopy as well. The upward and downward radiative fluxes are determined by the phase function of diffuse light, G-function, leaf reflectivity and transmisivity, leaf area index, and the cosine of solar angle of incident direct beam radiation (Zhou et al., 2018).

(e) Considering the wide distribution of rice paddies in Southeast Asia and the quite different characteristics of rice paddies and bare soil, a ~~simple~~ scheme to parameterize ~~about~~ the surface albedo, roughness length, turbulent sensible and latent heat fluxes over rice paddies is developed (a manuscript is in preparation) and implemented in BCC-AVIM2.0.

(f) Finally, land-use and land-cover changes are explicitly involved in BCC-AVIM2.0. An increase in crop area implies the replacement of natural vegetation by crops, which is often known as deforestation.

**2.3 Ocean and Sea Ice**

There are no significant changes for the ocean and sea ice from BCC-CSM1.1m to BCC-CSM2-MR. But for the sake of completeness, we present here a short description of them. The oceanic component is MOM4-L40, an oceanic GCM. It was based on the Z-coordinate Modular Ocean Model (MOM), version 4 (Griffies, 2005) developed by the Geophysical Fluid Dynamics Laboratory (GFDL). It has a nominal resolution of 1 °×1 °with a tri-pole grid, the actual resolution being from 1/3 ° latitude between 30 ℃S and 30 ℃N to 1.0 ° at 60 ° latitude. There are 40 z-levels in the vertical. The two northern poles of the curvilinear grid are distributed to land areas over Northern America and over the Eurasian continent. There are 13 vertical levels placed between the surface and the 300-m depth of the upper ocean. MOM4_L40 adopts some mature parameterization schemes, including Swedy's tracer-based third order advection scheme, isopycnal tracer mixing and diffusion scheme (Gent and McWilliams, 1990), Laplace horizontal friction scheme, KPP vertical mixing scheme (Large et al.,

1994), complete convection scheme (Rahmstorf, 1993), overflow scheme of topographic processing of sea bottom boundary/steep slopes (Campin & Goosse, 1999), and shortwave penetration schemes based on spatial distribution of chlorophyll concentration (Sweeney et al., 2005).

Concentration and thickness of sea ice are calculated by the Sea Ice Simulator (SIS) developed by GFDL (Winton, 2000). It is a global sea ice thermodynamic model including the Elastic–Viscous–Plastic dynamic process and Semtner's thermodynamic process. SIS has 3 vertical layers, including 1 snow cover and 2 ice layers of equal thickness. In each grid, 5 categories of sea ice (including open water) are considered, according to the thickness of sea ice. It also takes into account the mutual transformation from one category to another under thermodynamic conditions. The sea ice model operates on the same oceanic grid and has the same horizontal resolution of MOM_L40. SIS calculates concentration, thickness, temperature, salinity of sea ice and motions of snow cover and ice sheet. There is no gas exchange through sea ice.

**2.4. Surface turbulent fluxes between air and sea/sea ice**

The atmosphere and sea/sea ice interplay through the exchange of surface turbulent fluxes of momentum, heat and water. An optimum treatment of the surface exchange, sound in physics and economic in computation, is very important in simulating the climate variability. During the past years, we maintain a continuous effort to improve the turbulent exchange processes between air and sea/sea ice in different versions of BCC models.

In BCC-CSM1.1m, the bulk formulas of turbulent fluxes over sea surface originate from those used in CAM3, with some modifications to the roughness lengths and corrections to the temperature and moisture gradients considering sea spray effects (Wu et al., 2010). The bulk formulas are updated in BCC-CSM2-MR. The coefficients in roughness lengths calculations were adjusted and the arbitrary gradient corrections are not used. Instead, a gustiness parameterization is included to account for the subgrid wind variability that is contributed by boundary layer eddies, convective precipitation, and cloudiness (Zeng et al., 2002).

In terms of turbulent exchange between air and sea ice, we proposed a new bulk algorithm aiming to improve flux parameterizations over sea ice (Lu et al., 2013). Based on theoretical and observational analysis, the new algorithm employs superior stability functions for stable stratification as suggested by

Zeng et al. (1998), and features varying roughness lengths. All the three roughness lengths ($z_0$, $z_T$, $z_Q$) of sea ice were set to a constant (0.5 mm) in BCC-CSM1.1m. Observational studies show that values of $z_0$ tend to be smaller than 0.5 mm over sea ice in winter and larger than 0.5 mm in summer (Andreas et al., 2010a; Andreas et al., 2010b). In the new parameterization used in BCC-CSM2-MR, the roughness lengths for momentum differentiate between warm and cold seasons. For simplicity, $z_0$ is treated as

$$z_0(mm) = \begin{cases} 0.1 & \text{for } T_s \le -2°C \\ 0.8 & \text{for } T_s > -2°C \end{cases}, \quad (19)$$

where $T_s$ represents surface temperature. For the scalar roughness lengths, a theoretical-based model proposed by Andreas (1987) is used in the new scheme. This model expresses the scalar roughness $z_s$ ($z_T$ or $z_Q$) as a function of the roughness Reynolds number R*, i.e.,

$$\ln(z_s/z_0) = b_0 + b_1(\ln R_*) + b_2(\ln R_*)^2. \quad (20)$$

Andreas (1987, 2002) tabulates the polynomial coefficients $b_0$, $b_1$ and $b_2$.

## 3. Experimental design

All BCC sSimulations presented in this work follow the protocols defined by CMIP5 and CMIP6. We pay attention for them to be comparable in spite of showing the transition of our climate system model from CMIP5 to CMIP6. The principal simulation to be analyzed is the historical simulation (hereafter historical) with prescribed forcings from 1850 to 2005 for CMIP5 (to 2014 for CMIP6).

Historical forcings data are based as far as possible on observations and downloaded from the webpage (https://esgf-node.llnl.gov/search/input4mips/). They mainly include: (1) GHG concentrations (only $CO_2$, $N_2O$, $Ch_4$, CFC11, CFC12 used in BCC models) with zonal-mean values and updated monthly; (2) Yearly global gridded land-use forcing; (3) Solar forcing; (4) Stratospheric aerosols (from volcanoes); (5) CMIP6-recommended anthropogenic aerosol optical properties which is formulated in terms of nine spatial plumes associated with different major anthropogenic source regions (Stevens et al., 2017). (6) Time-varying gridded ozone concentrations. In addition, aerosol masses based on CMIP5 (Taylor et al., 2012) are used for on-line calculation of –cloud droplet effective radius in BCC model.

The preindustrial climateinitial state of BCC-CSM2-MR is preceded by a more than 500 –years piControl simulation following the requirement of CMIP6. The initial state of the piControl simulation itself is obtained through individual spin-up runs of each component of BCC-CSM2-MR in order for

piControl simulation to run stably and fast to its model equilibrium. Actually, the initial states of atmosphere and land are obtained from a 10-years AMIP run forced with monthly climatology of sea surface temperature (SST) and sea ice concentration, and the initial states of ocean and sea ice are derived from a 1000-years forced run with a repeating annual cycle of monthly climatology of atmospheric state from the Coordinated Ocean-Ice Reference Experiment (CORE) dataset version 2 (Danabasoglu et al., 2014). ~~.~~ Figure 2 shows time series of the annual and global mean of net energy flux at top of the atmosphere and the sea surface temperature for 600 years in the piControl simulation. The whole system in BCC-CSM2-MR nearly reaches its equilibrium after 600 years.

## 4. Evaluation and comparison between BCC CMIP5 and CMIP6 models

### 4.1 Global Energy Budget

Radiative fluxes at the top ~~up-limit~~ of the model atmosphere are fundamental variables characterizing the Earth's energy balance. Satellite observations in modern time allow us to monitor changes in the net radiation at top-of-atmosphere (TOA) from 2001 onwards. CERES (Clouds and Earth's Radiant Energy System) project, with the lessons learned from its predecessor, the Earth's Radiation Budget Experiment (ERBE), provides improved observation-based data products of Earth's radiation budget (Wielicki et al, 1996). Recently, data of CERES are synthesized with EBAF (Energy Balanced and Filled) data to derive the CERES-EBAF products, suitable for evaluation of climate models (Loeb et al., 2012). As shown in Table 4, the TOA shortwave and longwave components in BCC-CSM2-MR are generally closer to CERES-EBAF compared to those in BCC-CSM1.1m. Model results are for the period 1986–2005, while the available CERES-EBAF data are for 2003–2014. ~~With the CERES/EBAF data, we obtain a quasi-equilibrium (0.81 W m$^{-2}$) of Earth's radiative budget at TOA for the period of 2003 to 2014. As listed in Table 4, G~~globally-averaged TOA net energy is 0.85 W m$^{-2}$ in BCC-CSM2-MR and 0.98 W m$^{-2}$ in BCC-CSM1.1m for the period from 198~~61~~ to 200~~514~~. The energy equilibrium of whole earth system in BCC-CSM2-MR is slightly improved. ~~It means that the whole earth system in our models is very close to energy equilibrium. The TOA shortwave and longwave components in BCC-CSM2-MR are generally closer to CERES/EBAF than those in BCC-CSM1.1m.~~

带格式的：字体：（默认）Times New Roman，小四，字体颜色：自动设置

带格式的：字体：（默认）Times New Roman，小四，字体颜色：自动设置

带格式的：字体：（默认）Times New Roman，小四，字体颜色：自动设置

带格式的：字体：（默认）Times New Roman，小四，字体颜色：自动设置

带格式的：字体：（默认）Times New Roman，小四，字体颜色：自动设置

带格式的：字体：（默认）Times New Roman，（中文）+中文正文（宋体），小四

Clouds constitute a major modulator of the radiative transfer in the atmosphere for both solar and terrestrial radiations. Their macro and micro properties, including their radiative properties exert strong impacts on the equilibrium and variation of the radiative budget at TOA or at surface. Figure 3~~1~~ displays annual and zonal mean of shortwave, longwave and net cloud radiative forcing for BCC CMIP5 (blue curves), CMIP6 (red curves) models and observations (black curves). The data used in Fig. 3 are the same as in Table 4. ~~Model results are for the period 1986–2005, while the available CERES EBAF data are for 2003–2014.~~ Although observations and ~~the~~models results~~s~~ cover different time periods, they are still relevant to reveal climatological mean performance of climate models. In low latitudes between 30 °S and 30 °N, BCC-CSM1.1m shows excessive cloud radiative forcing for both shortwave and longwave radiations. These biases are largely reduced in BCC-CSM2-MR, which is possibly attributed to the new algorithm of cloud fraction especially for convective cloud amount. Cloud radiative forcing in ~~the~~ mid latitudes shows large uncertainty, also manifested in the large deviation between the two observations. Cloud radiative forcing in both models is closer to CERES-EBAF than to CERES in mid latitudes.~~in BCC-CSM2-MR seems, nevertheless, overestimated for the shortwave radiation.~~ It is clear that the new physics modifies the simulated climate and cloud properties, including the fractional coverage of clouds, their vertical distribution as well as their liquid water and ice content.

### 4.2. Performance in Simulating the Global Warming in the 20th Century

The historical simulation allows us to evaluate the ability of models to reproduce the global warming and climate variability in the 20th century. The performance depends on both model formulation and the time-varying external forcings imposed on the models (Allen et al., 2000). Figure 4 presents global-mean (from 60 °S to 60 °N) surface air temperature evolutions from HadCRUT4 (Morice et al., 2012) and BCC CMIP5 and CMIP6 models. Here only the area from 60° S to 60 °N is used for comparison, since few observations existed in polar regions to deduce reliable information in HadCRUT4, especially before the 20th century. To better reveal long-term trends, the climatological mean is calculated for the reference period 1961–1990 and removed from the time series. The interannual variability of both simulations is qualitatively comparable to that observed. When a 9-year smoothing is applied, the long-term trend of both CMIP6 and CMIP5 models is highly correlated with

HadCRUT4. Figure 4 presents three members of historical simulations from different initial state of the piControl simulation. The correlation coefficients are 0.90 in CMIP5 and 0.93, 0.93, 0.90 in three members of CMIP6, respectively.

A remarkable feature in Figure 4 is the presence of a global warming hiatus or pause for the period from 1998 to 2013 when the observed global surface air temperature warming slowed down. This is a hot topic, largely debated in the scientific research community (e.g. Fyfe et al., 2016; Medhaug et al., 2017). There are two members (r1i1p1f1 and r2i1p1f1 in Fig. 4) of historical simulations of the CMIP6 model show a hiatus towards the end of the simulation that resembles the observed one, and the third member (r3i1p1f1) shows a decreased trend of warming in the same period. Another warming hiatus occurred in the period of 1942 to 1974. The first and the third members (r1i1p1f1 and r3i1p1f1) of BCC-CSM2-MR only simulate the warming slowdown in the late period from 1958 to 1974, but the second member (r2i1p1f1) of BCC-CSM2-MR almost simulate this warming hiatus in the whole period from 1942 to 1974. The reason why the BCC CMIP6 model simulates both periods of global warming hiatus is beyond the scope of this paper and will be explored in future.

The models response of the SAT to volcanic forcing is slightly stronger than that estimated with HadCRU data. Evident global cooling shocks are coincident with significant volcanic eruptions such as Krakatoa (in 1883), West Indies Agung (in 1963), and Mount Pinatubo (in 1991). Each of these volcanic eruptions significantly enriched stratospheric aerosols (available from http://data.giss.nasa.gov/modelforce/strataer/). As shown in Figure 4, SAT may decrease by up to 0.4 ℃ within 1 to 2 years after major volcanic eruptions. The substantial cooling response to volcanic eruptions is, to a great extent, due to the aerosol direct radiative forcing too strong in both versions of BCC-CSM.

To keep the paper concise and at a reasonable length, only the first member of CMIP6 historical simulations of BCC-CSM2-MR will be presented hereafter. Biases of annual mean surface air temperature (at 2 meters) in the whole globe for BCC-CSM2-MR and BCC-CSM1.1m are shown in Figure 5. In both BCC models, biases are generally within ±3 ℃, but there are slightly systematic warm biases over oceans from 50 ℃S to 50 ℃N and systematic cold ones over most land regions in north of 50 ℃N, in East Asia and in North Africa. Cold biases in high latitudes of the Northern Hemisphere

带格式的：字体：小四，字体颜色：自动设置

带格式的：缩进：首行缩进： 1.5 字符

(North Atlantic, Arctic, North America and Siberia) seem amplified in BCC-CSM2-MR. The land surface biases in both coupled models are similar to each other. Those patterns of biases are already present in AMIP simulations (not shown), where effects of oceanic biases are excluded. So those biases in land surface partly come from their land surface modelling component. In the Southern Ocean, both models show a strong warm area in the Weddell Sea. BCC-CSM1.1m shows cold biases in other regions of the Southern Ocean. The disappearance of cold biases in the Southern Oceans in BCC-CSM2-MR is possibly attributed to the new scheme of cloud fraction (Table 2) as there is a zone of low-level cloud between 40 ℃S to 60 ℃S in the Southern Ocean (omitted), not only in models but also in observations.

### 4.3 Climate sensitivity to $CO_2$ increasing

The long trend of global warming in Figure 4 depends on the climate sensitivity which is an emblematic parameter to characterize the sensitivity of a climate model to external forcing, with all feedbacks included. It generally designates the variation of global mean surface air temperature in response to a forcing of doubled $CO_2$ concentration in the atmosphere (IPCC 2013). As commonly practiced in the climate modelling community, an equilibrium climate sensitivity and a transient climate response can be separately evaluated, corresponding to a situation of equilibrium and transient states of climate.

We use the standard simulation of 1% $CO_2$ increase per year (1pct$CO_2$) to calculate the transient climate response (TCR), while the equilibrium climate sensitivity (ECS) uses the 4x$CO_2$ abrupt-change simulation by applying the forcing/response regression methodology proposed by Gregory et al. (2004). The TCR is calculated using the difference of annual surface air temperature between the pre-industrial experiment and a 20-year period centered on the time of $CO_2$ doubling in 1pct$CO_2$, which is 1.71 for BCC-CSM2-MR and 2.02 for BCC-CSM1.1m. The ECS is diagnosed from the 150-year run of abrupt 4xCO2 following the approach of Gregory (2012). The method is based on the linear relationship (Figure 6) governing the changes of net top-of-atmosphere downward radiative flux and the surface air temperature simulated in abrupt 4x$CO_2$ relative to the pre-industrial experiment. The ECS is equal to a half of the temperature change when the net downward radiative flux reaches zero (Andrews et al., 2012). It is assumed here that 2x$CO_2$ forcing is half of that for 4x$CO_2$, hypothesis generally verified in

climate models. As shown in Fig. 6, the ECS is 3.03 for BCC-CSM2-MR and 2.89 for BCC-CSM1.1m. So the TCR of the new version model BCC-CSM2-MR is lower than BCC-CSM1.1m, but the ECS of BCC-CSM2-MR is slightly higher than BCC-CSM1.1m.

The linear regression line shown in Figure 6, as pointed out in Gregory et al. (2012), also allows estimating the instantaneous forcing due to $CO_2$ increase, and eventually feedbacks parameter of the climate system. The former is the cross point of the linear regression line with Y axis: 6.2 $W_{\blacktriangle} \cdot m^{-2}$ for BCC-CSM2-MR and 7.6 $W\ m^{-2}_{\blacktriangle}$ for BCC-CSM1.1m. They can be scaled to the case of $2xCO_2$ just with a division factor of 2. Since ECS values are close to each other in the two models, we can easily deduce that all-feedback factor is larger in BCC-CSM2-MR than in BCC-CSM1.1m. It is actually not surprising to see differences of $2xCO_2$ radiative forcing between the two models even the radiative transfer scheme is kept identical, because changes in 3-D structures of cloud, atmospheric temperature and water vapor do exert impacts on additional radiative forcing due to $CO_2$ increase in the atmosphere. It is however interesting to note that feedbacks can operate, in the two models, in such a different way that ECS keeps almost unchanged between them.

带格式的：下标
带格式的：字体：Times New Roman
带格式的：上标
带格式的：下标
带格式的：下标
带格式的：下标

**4.~~4~~2 Behaviors of the atmosphere at present day**

~~Biases of annual mean surface air temperature (at 2 meters) for BCC-CSM2-MR and BCC-CSM1.1m are shown in Figure 2. In both BCC models, biases are generally within ±3 ℃, but there are slightly systematic warm biases over oceans from 50 ℃S to 50 ℃N and systematic cold ones over most land regions in north of 50 ℃N, in East Asia and in North Africa. Cold biases in high latitudes of the Northern Hemisphere (North Atlantic, Arctic, North America and Siberia) seem amplified in BCC-CSM2-MR. In the Southern Ocean, both models show a strong warm area in the Weddell Sea. BCC-CSM1.1m shows cold biases in other regions of the Southern Ocean.~~ The main spatial patterns of observed precipitation climatology are simulated in BCC-CSM1.1m and BCC-CSM2-MR.

Figure ~~7~~3 shows model biases of annual-mean precipitation for BCC-CSM1.1m and BCC-CSM2-MR in the globe. They are very close from each other. Their RMSE is also very close: 1.12 mm/day against 1.18 mm/day. Regions of lack of precipitation, such as North India, South China, the two sides of Sumatra, and the Amazon, experience significant amelioration in the new model. Excessive rainfalls in Tropical Africa, in the Indian Ocean, in the Maritime Continent seem amplified in

BCC-CSM2-MR. As for the whole globe, the annual mean precipitation coming from convective process (including deep and shallow convections) accounts for 50% of the total precipitation (2.94 mm/day) in BCC-CSM2-MR and 48% of the total precipitation (2.87 mm/day) in BCC-CSM1.1m. The convective precipitation increased in BCC-CSM2-MR, and the total amount of precipitation exceeds the amount (2.68 mm/day) of 1986-2005 mean observed precipitation analyses from Global Precipitation Climatology Project (Adler et al., 2003). But in some regions such as in the Maritime Continent, stratus precipitation evidently enhances in BCC-CSM2-MR, where the ratio of convection precipitation to total precipitation is 39% and even larger than 35% in BCC-CSM1.1m.

~~. Regions of lack of precipitation, such as North India, South China, the two sides of Sumatra, and the Amazon, experience significant amelioration in the new model.~~

We now use the Taylor diagram (Figure 8~~4~~) to evaluate the general performance of our two models in terms of temperature at 850hPa, precipitation and atmospheric general circulation. The evaluation is done against climatology of ERA-Interim dataset for the period of 1986 to 2005 (~~-~~Dee et al., 2011). ERA-Interim is the latest global atmospheric reanalysis produced by the European Centre for Medium - Range Weather Forecasts (ECMWF).

For global fields, we calculate the spatial pattern correlations between models and ERA-Interim ~~NCEP~~ dataset for the annual-mean climatology of sea level pressure (SLP), ~~precipitation (PRCP),~~ temperature at 850 hPa level (T850), wind velocity at 850 hPa (U850 and V850) and at 200 hPa (U200), and geopotential height at 500hPa (Z500)~~ over the period 1980-2000~~, and Global Precipitation Climatology Project dataset of precipitation (PRCP in Fig. 8, Adler and Chang, 2003) over the period 1980–2000. Except for precipitation and zonal wind at 850 hPa which have lower correlation (less than 0.90) with observation, correlations for other variables are all above 0.90. The pattern correlation of geopotential height at 500hPa with ERA-Interim~~NCEP~~ is 0.995, the best correlation among these variables. Except for V850, correlations of all other variables in CMIP6 model version (BCC-CSM2-MR) have an evident improvement compared to CMIP5 version (BCC-CSM1.1m). The normalized standard deviations of most variables except for the precipitation and T850 are obviously improved in BCC-CSM2-MR. As a whole, the performances of most variables in BCC-CSM2-MR are better than those in BCC-CSM1.1m.

Results shown in the Taylor diagrams in Figure 84s about improvements in surface climate and atmospheric general circulation at different vertical levels are consistent with improvements in the vertical distribution of atmospheric temperature. Figure 59 shows the yearly-averaged zonal mean of atmospheric temperature biases in BCC-CSM2-MR and BCC-CSM1.1m, with ERA-Interim for the period of 1986–2005 as reference. Overall, both BCC-CSM2-MR and BCC-CSM1.1m have similar biases in their vertical structure, with 1–3 K warmer in the stratosphere (above 100 hPa) for most of the domain equatorward of 70 ℃N and 70 ℃S. There are larger cold biases near the tropopause (centered near 200hPa) for southward of 30 ℃S and northward of 30 ℃N. In the middle to lower troposphere (below 400hPa), there is a warm bias of 1-2K. Improvements in BCC-CSM2-MR are mainly located in the troposphere below 100 hPa. Both cold biases near the tropopause in high latitudes and warm bias in lower latitudes are reduced.

The improvement in tropospheric temperature induces naturally smaller biases for the zonal wind in the whole troposphere in BCC-CSM2-MR (Figure 95). But there are still westerly wind biases of 6 $m \cdot s^{-1}$ in the layer of 100-200 hPa in the tropics. Westerly jets at mid-latitudes are slightly too strong in both hemispheres. The zonal mean of zonal wind biases in the high latitudes of the stratosphere in BCC-CSM2-MR have increased near 10 hPa, where model biases may be partly caused by not yet involved gravity wave drag that generated by blocking effects. We expect to reduce this model bias in next version by adding this process of gravity wave drag.

带格式的: 字体: Times New Roman

Given a much higher vertical resolution and an advanced parameterization of the gravity wave drag, the new model BCC-CSM2-MR is able to represent the stratospheric quasi-biennial oscillation (QBO), as shown in Figure 106 which displays time-height diagrams of the tropical zonal winds averaged from 5 ℃S to 5 ℃N. The three panels show observations from the ERA-Interim reanalysis and relevant simulation results from the two models in CMIP6 and CMIP5. Figure 106(a) shows alternative westerlies and easterlies in the lower stratosphere appearing with a mean period of about 28 months in the ERA-Interim reanalysis. In Figure 106(b), the BCC-CSM2-MR simulations present a clear quasi-biennial oscillation of the zonal winds as observed. In this study, the QBO period is taken as the time between easterly and westerly wind transitions at 20 hPa. The simulation produces about 12 QBO cycles from 1980 to 2005. The average period is 24.6 months, whereas the shortest and longest cycles

last for 18 and 35 months, respectively. ERA-Interim values are 27.9, 23, and 35 months for average, minimum, and maximum of cycle length. The observed asymmetry in amplitude with the easterlies being stronger than the westerlies is reproduced in the simulated zonal winds. At 20 hPa, the simulated easterlies often exceed -20 m ~~·~~s$^{-1}$, while in the reanalysis easterly winds peak at -30 to -40 m ~~·~~s$^{-1}$. Simulated westerlies of the QBO range from 8 to 12 m ~~·~~s$^{-1}$, whereas the reanalysis show peak winds of 16 to 20 m ~~·~~s$^{-1}$. The amplitudes of the QBO cycles in the simulation are weaker than in the reanalysis, which is possibly due to ~~implying that the~~ inadequate gravity wave forcing ~~is less adequate~~ to drive the QBO. The downward propagation of the simulated QBO phases occurs in a regular manner, but does not penetrate to sufficiently low altitudes. It may depend~~s~~ on the vertical resolution and ~~will discuss~~ the impact of vertical resolution on downward propagation will be discussed in a separate paper. After a few test of model vertical layers, we tend to conclude that 46 vertical layers (Figure 1) seem the minimum number to simulate QBO in BCC-CSM2-MR. In ~~the~~ BCC-CSM1.1m, however, ~~simulations~~ as shown in Figure 10~~6(c)~~, ~~however, the~~ QBO is inexistent and only a semiannual oscillation of easterlies can be found.

Madden-Julian Oscillation (MJO) is a very important atmospheric variability acting within a periodicity between 20 and 100 days in the tropics with considerable effects on regional weather and climate. It exerts significant impacts on monsoonal circulations and organization of tropical rainfalls. From the tropical Indian Ocean to the Western Pacific, MJO shows a pronounced behavior of eastward propagation, as shown in Figure 11~~7~~a, in the form of longitude-time, the lagged correlation coefficient of the rainfall in the eastern Indian Ocean (75–85 °E; 5 °S–5 °N) with other positions and with lagged time. We can easily observe the eastward-propagating characteristic, with a moving velocity estimated at 5 m ~~·~~s$^{-1}$. As shown in a comparison work of Jiang et al. (2015), three fourth of CMIP5 models don't show the propagation behavior, with only a standing oscillation when data are filtered to retain only the 20-100 day variability. Figure 11~~7~~b and 11~~7c~~c show the same plot, but from our two models in CMIP5 and CMIP6. Although the new model is far from realistic in terms of eastward propagation, there is indeed a clear improvement compared to the old one.

MJO can also exert impacts on weather and climate of extra-tropics, either through emanation of Rossby waves, or the poleward propagation of MJO itself. Figure 11~~7~~d shows a latitude-time diagram

for lagged correlation coefficients when rainfalls are filtered to only retain the variability of 20-100 days. Panels ~~Figure 7~~e and ~~7~~f in Figure 11 are the counterpart simulated by our two models. The new model presents a clear improvement.

### 4.5 Interannual variation of sea surface temperature (SST) in the equatorial Pacific

Figure 12 shows the observed and simulated spatial pattern of standard deviation of SST anomalies in the tropical Pacific. Both BCC-CSM2-MR and BCC-CSM1.1m can simulate the position of the strongest variation of SST, situated in the central-eastern Pacific in the east of the dateline. However, cold SST in the eastern equatorial Pacific still extends too far west in both models and a cold tongue bias exists in the equatorial Pacific (not shown). As shown in Figure 12a, HadISST observations (Rayner et al., 2003) can clearly identify a zone of large interannual variation of SST from the Peruvian coast to the equatorial cold tongue. It is well simulated in BCC-CSM2-MR, but almost missing in BCC-CSM1.1m.

Figure 13 presents time series of the monthly Nino3.4 SST Index from observations and from simulations of BCC-CSM1.1m and BCC-CSM2-MR. Although amplitudes of interannual variations of the Nino3.4 index in both models are larger than in HadISST observations, it gets weaker in BCC-CSM2-MR with standard deviation of 0.91℃ which is close to observation showing standard deviation of 0.79℃. Recent studies of Lu and Ren (2016) reveal that the period ENSO periodicity in BCC-CSM1.1m is only 2.4 years, much shorter than that in observation. This bias of a too-short periodicity of the ENSO cycle still persists in BCC-CSM2-MR. Lu and Ren (2016) furthermore pointed out that this ENSO periodicity bias in BCC-CSM1.1m is likely caused by an underestimated air-sea coupling strength, and consequently too-weak response of the equatorial Pacific surface westerly wind to SST warm phase in the eastern Pacific. This can affect and distort the zonal advective feedback and thermocline feedback which are two crucial mechanisms for the phase transition of ENSO.

### 4.6 ~~3~~ Sea ice state and oceanic overturning circulation~~—~~

Figure 14 shows time-series of minimum sea-ice extent from 1851 to 2012 for (a) the Arctic in September and (b) the Antarctic in March as simulated in BCC-CSM2-MR and BCC-CSM1.1m. As the NSIDC data we have are from 1979 to 2010, which are not long enough to meet our needs here, observation-based HadISST sea ice data, instead of NSIDC data, are plotted when available, where sea

带格式的: 行距：1.5 倍行距，无孤行控制，图案：清除
带格式的: 字体：（中文）宋体，小四
带格式的: 字体：（中文）+中文正文（宋体），字体颜色：自动设置
带格式的: 字体：（中文）+中文正文（宋体），字体颜色：自动设置
带格式的: 字体：（中文）+中文正文（宋体），字体颜色：自动设置
带格式的: 字体：（中文）+中文正文（宋体），字体颜色：自动设置
带格式的: 字体：小四，字体颜色：自动设置
带格式的: 字体：（中文）+中文正文（宋体），字体颜色：自动设置
带格式的: 字体：（中文）+中文正文（宋体），字体颜色：自动设置
带格式的: 字体：（中文）+中文正文（宋体），字体颜色：自动设置
带格式的: 字体：（中文）+中文正文（宋体），字体颜色：自动设置
带格式的: 字体：（中文）+中文正文（宋体），字体颜色：自动设置
带格式的: 字体：（中文）+中文正文（宋体），字体颜色：自动设置
带格式的: 字体：（中文）+中文正文（宋体），字体颜色：自动设置
带格式的: 字体：（中文）+中文正文（宋体），字体颜色：自动设置
带格式的: 字体：（中文）+中文正文（宋体），字体颜色：自动设置
带格式的: 字体：（中文）+中文正文（宋体），字体颜色：自动设置
带格式的: 字体：（中文）+中文正文（宋体），字体颜色：自动设置
带格式的: 字体：（中文）+中文正文（宋体），字体颜色：自动设置
带格式的: 字体：（中文）+中文正文（宋体），字体颜色：自动设置
带格式的: 字体：（中文）+中文正文（宋体），字体颜色：自动设置
带格式的: 字体：（中文）+中文正文（宋体），字体颜色：自动设置
带格式的 ...

ice extent are computed from sea ice concentration. The Arctic sea-ice extent in BCC-CSM2-MR is slightly improved, in comparison to BCC-CSM1.1m. But the Antarctic minimum sea-ice extent in the new model is very small, almost a third of what observed. The old model had however a more realistic behavior for this regard. This discrepancy is related to too-warm temperatures simulated in BCC-CSM2-MR in the Southern Ocean, in particular in the Weddell Sea. The downward trend in the Arctic summer sea-ice extent is, however, better simulated in the new model than in the old one.

Figure 15~~8~~ shows the seasonal cycle of sea ice extent (SIE) and thickness in the two Polar Regions in our models. Observations from the National Snow and Ice Data Center (NSIDC) and the European Centre for Medium-Range Weather Forecasts (ECMWF) are also plotted for the purpose of comparison. Observations from NSIDC show that Arctic sea ice cover reaches a minimum extent of $7.74\times10^6$ km$^2$ in September and rises to a maximum extent of $15.79\times10^6$ km$^2$ in March (Fig. 15~~8~~a). The two models can both capture the seasonal variation and pattern, but large biases exist in magnitude, especially in boreal winter. As to Antarctic SIE, the ice cover undergoes a very large seasonal cycle, which is similar to observations. However, the SIE in BCC-CSM1.1m is too extensive throughout the year, particularly in southern hemisphere winter. Comparatively, the new model BCC-CSM2-MR simulates a relatively smaller seasonal cycle and reduced ice cover in all months which is closer to observations. As to ice thickness, the two models simulate a thinner ice cover compared to observations in all seasons for both Arctic and Antarctic. The most remarkable improvements of BCC-CSM2-MR appear in the boreal warm seasons, especially from June to September with thicker ice presented in the Arctic Ocean. Those improvements may be partly achieved with the new model physics such as schemes for turbulent flux over sea ice and ocean surfaces, cloud fraction, or atmospheric circulation improvements at high latitudes.

The Atlantic Meridional Overturning Circulation (AMOC) plays a significant role in driving the global climate variation (Caesar et al., 2018). AMOC consists of two primary overturning cells. In the upper cell, warm water flows northward in the upper 1000 m to supply the formation of the North Atlantic Deep Water (NADW), which returns southward in the depth range of approximately 1500 to 4000 m. In contrast, in the lower cell, the Antarctic Bottom Water (AABW) flows northward in the Atlantic basin beneath NADW. Figure ~~9~~16 shows the time-averaged AMOC simulated by the two

coupled model versions. The two main cells are well depicted. The lower branch of NADW is much deeper in BCC-CSM2-MR than in BCC-CSM1.1m, as indicated by the depth of the zero-contour line. Moreover, the central intensity of NADW in BCC-CSM2-MR is over 22.5 Sv ~~,~~ ~~–~~about 2.5 Sv stronger than that in BCC-CSM1.1m, close to observation-based value (25 Sv in Talley et al., 2013).~~–~~

带格式的：缩进：首行缩进： 0 字符

~~**4.4. Performance in Simulating the Global Warming in the 20th Century**~~

~~The historical simulation allows us to evaluate the ability of models to reproduce the global warming and climate variability in the 20th century. The performance depends on both model formulation and the time varying external forcings imposed on the models (Allen et al., 2000). Figure 10 presents global mean (from 60° S to 60 °N) surface air temperature evolutions from HadCRUT4 (Morice et al., 2012) and BCC CMIP5 and CMIP6 models. To better reveal long term trends, the climatological mean is calculated for the reference period 1961–1990 and removed from the time series. The interannual variability of both simulations is qualitatively comparable to that observed. When a 9 year smoothing is applied, the long term trend of both CMIP6 and CMIP5 models is highly correlated with HadCRU. The correlation coefficients are 0.90 in CMIP5 and 0.93 CMIP6, respectively.~~

~~A remarkable feature in Figure 10 is the presence of a global warming hiatus or pause for the period from 1998 to 2013 when the observed global surface air temperature warming slowed down. This is a hot topic, largely debated in the scientific research community (e.g. Fyfe et al., 2016; Medhaug et al., 2017). Our CMIP6 model can capture this warming hiatus. Another warming hiatus occurred in the period of 1942 to 1974. BCC models only capture the warming slowdown in the late period from 1958 to 1974. The reason why the BCC CMIP6 model captures both periods of global warming hiatus will be explored in other paper.~~

~~The models response of the SAT to volcanic forcing is slightly stronger than that estimated with HadCRU data. Evident global cooling shocks are coincident with significant volcanic eruptions such as Krakatoa (in 1883), West Indies Agung (in 1963), and Mount Pinatubo (in 1991). Each of these volcanic eruptions significantly enriched stratospheric aerosols (available from http://data.giss.nasa.gov/modelforce/strataer/). As shown in Figure 2c, SAT may decrease by up to 0.4 ℃ within 1 to 2 years after major volcanic eruptions. The substantial cooling respone to volcanic~~

eruptions is, to a great extent, due to the aerosol direct radiative forcing too strong in both versions of BCC-CSM.

Figure 11 shows time series of minimum sea ice extent from 1851 to 2012 for (a) the Arctic in September and (b) the Antarctic in March as simulated in BCC-CSM2-MR and BCC-CSM1.1m. Observation-based NSIDC data are also plotted when available. The Arctic sea-ice extent in BCC-CSM2-MR is slightly improved, in comparison to BCC-CSM1.1m. But the Antarctic minimum sea ice extent in the new model is very small, almost a third of what observed. The old model had however a more realistic behavior for this regard. This discrepancy is related to too warm temperatures simulated in BCC-CSM2-MR in the Southern Ocean, in particular in the Weddell Sea. The downward trend in the Arctic summer sea ice extent is, however, better simulated in the new model than in the old one.

**4.5 Climate sensitivity to $CO_2$ increasing**

Climate sensitivity is an emblematic parameter to characterize the sensitivity of a climate model to external forcing, with all feedbacks included. It generally designates the variation of global mean surface air temperature in response to a forcing of doubled $CO_2$ concentration in the atmosphere (IPCC 2013). As commonly practiced in the climate modelling community, an equilibrium climate sensitivity and a transient climate response can be separately evaluated, corresponding to a situation of equilibrium and transient states of climate.

We use the standard simulation of 1% $CO_2$ increase per year (1pct$CO_2$) to calculate the transient climate response (TCR), while the equilibrium climate sensitivity (ECS) uses the 4x$CO_2$ abrupt change simulation by applying the forcing/response regression methodology proposed by Gregory et al. (2004). The TCR is calculated using the difference of annual surface air temperature between the pre industrial experiment and a 20-year period centered on the time of $CO_2$ doubling in 1pct$CO_2$, which is 1.71 for BCC-CSM1.1m and 2.02 for BCC-CSM2-MR. The ECS is diagnosed from the 150 year run of abruptCO2 following the approach of Gregory (2012). The method is based on the linear relationship (Figure 12) governing the changes of net top of atmosphere downward radiative flux and the surface air temperature simulated in abrupt 4x$CO_2$ relative to the pre industrial experiment. The ECS is equal to a half of the temperature change when the net downward radiative flux reaches zero (Andrews et al.,

~~2012). It is assumed here that 2x$CO_2$ forcing is half of that for 4x$CO_2$, hypothesis generally verified in climate models. As shown in Fig. 12, the ECS is 3.03 for BCC-CSM2-MR and 2.89 for BCC-CSM1.1m. So the TCR of the new version model BCC-CSM2-MR is lower than BCC-CSM1.1m, while the ECS of BCC-CSM2-MR is higher than BCC-CSM1.1m.~~

**4.~~7~~6 ~~.~~ Evaluation of models for their performance in East Asia**

A good simulation of climate over East Asia is always a challenging issue for the climate modelling community, as the region is under influences of complex topography (high Tibetan Plateau), and atmospheric circulations from low latitudes (tropical monsoon circulation) and from higher latitudes. Figure 1~~7~~3 plots a Taylor diagram to show models performance of main climate variables over East Asia covering the region (100°-140°E, 20°-50°N). Both BCC-CSM1.1m (blue figures) and BCC-CSM2-MR (red figures) are plotted for precipitation, sea-level pressure and variables of the atmospheric general circulation. There is a clear and remarkable improvement from ~~BCC~~ CMIP5 to CMIP6 in BCC models. The amelioration is both in the spatial pattern correlation (radial lines) and in the ratio of standard deviations (circles from the origin).

Figure 18 shows the 1980-2005 climatology of December-January-February and June-July-August averaged precipitation over China and its surroundings. In boreal winter, GPCP precipitations show a rain belt from Southeast China to Japan and another rain belt along the southwestern flank of the Tibetan Plateau. In BCC-CSM1.1m the winter precipitation is too weak in Southeast China and too strong near Japan, compared to GPCP observations. This rain belt in BCC-CSM2-MR obviously spreads westward and is much closer to observations. The rain belt along the southwestern flank of the Tibetan Plateau in BCC-CSM2-MR, however, gets too strong. In boreal summer, large dry biases over East China are present in BCC-CSM1.1m. Those biases are reduced in BCC-CSM2-MR. The center of precipitation around Japan is also well simulated in BCC-CSM2-MR.

The East Asian summer monsoon rainfall has a seasonal progression from south to north at the beginning of summer and then a quick retreat to the south when the summer monsoon terminates (as shown in Figure 1~~9~~4a). This phenomenon is strongly related to the fact that the East Asian monsoon rainfall mainly takes place in the frontal zone between warm and humid air mass from the south, and cold and dry air mass from the north. This seasonal migration is also accompanied with a meridional

movement of the Western North Pacific Subtropical High, an important atmospheric center of action controlling the climate of the region. In Figure 19 (panels ~~4~~b and ~~14~~c), we compare the ~~our~~ two models in terms of seasonal migration of the monsoon rainfall. In the old model, rainfall was too weak. The new model produces more precipitation. In terms of seasonal match, both models show a delay of the peak rainfall by about one month, even longer in BCC-CSM2-MR.

Finally, let us examine the rainfall diurnal cycle in summer. Figure 20~~15~~ shows the timing of the rainfall diurnal cycle from observation and the two models. Main zones of nocturne rainfall can be recognized in the south flank of the Tibetan Plateau, in the Sichuan Basin in the east of the Tibetan Plateau, and in the north of Xinjiang in Central Asia. There is also a zone of nocturne rainfall in the low reach of the Yellow River. This is mainly under the influence of nocturne rainfall in the area of the Bohai Sea. Other regions over land experience diurnal rainfall peak in the afternoon after 16 hours local time. The diurnal cycle of rainfall was extensively studied in Jin et al. (2013) in terms of physics causing the diurnal cycle. But the good simulation of diurnal cycle is always a major challenge for climate modeling. We can see that it is not very well simulated in our old model and in East China the peak occurs in the mid and later night (0-4 am). But the improvement is quite spectacular in our new model with rainfall peak delayed in the afternoon. Such an improvement is due to the implementation of our new trigger scheme in convection parameterization.

## 5. Conclusions and discussion

This paper presents the main progress of BCC climate system models from CMIP5 to CMIP6 and focuses on the description of CMIP6 version ~~model~~ BCC-CSM2-MR and CMIP5 version ~~model~~ BCC-CSM1.1m especially on the model physics. Main updates in model physics include a modification of deep convection parameterization, a new scheme for cloud fraction, indirect effects of aerosols through ~~on~~ clouds and precipitation, and the gravity wave drag generated by deep convection. Surface processes in BCC-AVIM have also been significantly improved for soil water freezing treatment, snow aging effect on surface albedo, and timing of vegetation leaf unfolding, growth, and withering. A four-stream radiation transfer within the vegetation canopy ~~is used to~~ replaced the two-stream radiation transfer. There is a new treatment for rice paddy waters. New schemes for surface turbulent fluxes of momentum, heat and water at ~~in~~ the interface of atmosphere and sea/sea ice are also used.

The evaluation of model performance in simulating present-day climatologye is presented for main climate variables, such as, surface air temperature, precipitation, and atmospheric circulation for the globe and for East Asia. Emphasis is put on comparison between the CMIP5 and CMIP6 model versions (BCC-CSM2-MR versus BCC-CSM1.1m). The globally-averaged TOA net energy budget is 0.85 W • $m^{-2}$ in BCC-CSM2-MR, and 0.98 W -$m^{-2}$ in BCC-CSM1.1m. Both versions have a very good energy equilibrium. Model biases of excessive cloud shortwave and longwave radiative forcings over low latitudes in BCC-CSM1.1m are obviously reduced in BCC-CSM2-MR. When Taylor diagrams are used to compared the two models for spatial patterns of main climate variables such as with BCC-CSM1.1m, the spatial patterns of climate means of 2-meter surface air temperature, precipitation, and atmospheric general circulation, in BCC-CSM2-MR shows an are overall improvemented at both at the global scale and , particularly at the regional scale in East Asia. These improvements in BCC-CSM2-MR are possibly caused by usage of believed to be achieved by the a new scheme of for cloud fraction and by the consideration of indirect effects of aerosol on clouds and precipitation. The details will be discussed in the other paper. The cold tongue bias of SST in the equatorial Pacific in BCC-CSM1.1m still exists in BCC-CSM2-MR. BCC-CSM1.1m has a severe bias in sea ice extent (SIE) and thickness (Tan et al., 2015): too extensive in cold seasons and less extensive in warm seasons in both hemispheres. The most impressive improvements in BCC-CSM2-MR appear in the boreal warm seasons, especially from June to September with thicker ice presented in the Arctic Ocean. However, in the Southern Hemisphere, the sea ice extent and thickness in BCC-CSM2-MR become even systematically smaller than those in its previous version. This is still an issue that needs to be addressed in our the future work. There is another model bias of weak oceanic overturning circulation in BCC-CSM1.1m. This bias is reduced in the new version BCC-CSM2-MR, and the strength of AMOC is increased.

Further evaluations are performed on climate variabilities at different time scales, including long-term trend of global warming in the 20$^{th}$ century, QBO, MJO, and diurnal cycle of precipitation. The globally-averaged annual-mean surface air temperature from the historical simulation of BCC-CSM2-MR is much closer to HadCRUT4 observation than BCC-CSM1.1m, and the observed global warming hiatus or warming slowdown in the period from 1998 to 2013 is captured in some

带格式的: 字体: Times New Roman

realization of BCC-CSM2-MR. With a higher vertical resolution and ~~the~~ inclusion of the gravity wave drag generated by deep convection, the new version ~~of~~ BCC-CSM2-MR is able to reproduce the stratospheric QBO, while QBO even ~~it~~ does not exist in BCC-CSM1.1m. Further investigations on physical mechanisms controlling QBO simulation in BCC-CSM2-MR ~~is related to not only high resolution in the vertical layers but also consideration of gravity wave drag generated by deep convection. It will be discussed in Lu et al. (to be submitted)~~ will be reported in future. MJO is a very important atmospheric oscillation at intra-seasonal scales and main features are ~~partly~~ reproduced and improved in BCC-CSM2-MR, but with ~~its~~ intensity ~~is~~ still weaker than its counterpart in observation. At interannual scale, BCC-CSM1.1m shows too-strong variations of Nino 3.4 SST index, but too-short and too-regular periodicity for ENSO. BCC-CSM2-MR shows weaker amplitude for Nino 3.4 SST index, which is an improvement and closer to HadISST observations. The rainfall diurnal cycle in China has strong regional variations with pronounced nocturne rainfalls in the Sichuan Basin and in north China near the Bohai Sea and the coast. The diurnal rainfall generally peaks in the local time afternoon for most other land regions. BCC-CSM2-MR shows a clear improvement of rainfall diurnal peaks compared to the CMIP5 model (BCC-CSM1.1m). This improvement of rainfall diurnal variation is strongly ~~partly~~ related to the modification of deep convecti on~~ve~~ scheme ~~of Wu (2012), which will be discussed in the other paper~~.

Finally, we also evaluate the climate sensitivity to $CO_2$ increasing in the standard simulation of 1% $CO_2$ increase per year (1pctCO2) and the 4xCO2 abrupt-change. The transient climate response in the new CMIP6 model version BCC-CSM2-MR is lower than that in the previous CMIP5 model BCC-CSM1.1m, while the equilibrium climate sensitivity ECS for BCC-CSM2-MR is slightly higher than its counterpart in BCC-CSM1.1m.

From our model evaluations, we find that although basic feature of the QBO can be simulated in BCC-CSM2-MR, the magnitude between westerly and easterly interchange is still too weak. We also note that there are large biases of air temperature and winds in the stratosphere. Therefore, improvement of the stratospheric temperature and circulation simulations is an important priority in the future development of BCC models. In addition, sea ice simulation in the Antarctic region has large biases, which need to be improved.

## 6. Code and data availability

Source codes of BCC models are freely available upon request addressed to ~~Please contact~~ Tongwen Wu (twwu@cma.gov.cn) ~~to obtain the source codes for BCC models~~. ~~The m~~Model output of BCC models for both CMIP5 and ~~from the~~ CMIP6 ~~historical~~ simulations described in this paper ~~will be~~ is distributed through the Earth System Grid Federation (ESGF) and~~. As for BCC CMIP5 simulation, the model output will be freely~~ freely accessible through the ESGF data portals after registration. Details about ESGF are presented on the CMIP Panel website at http://www.wcrp-climate.org/index.php/wgcm-cmip/about-cmip.

**Author contributions**

Tongwen Wu le~~a~~d the BCC-CSM development. Tongwen Wu and Xiaoge Xin designed the experiments and carried them out. Tongwen Wu, Laurent Li, and Xiaohong Liu wrote the final document with contributions from all other authors.

**Acknowledgements**

This work was supported by The National Key Research and Development Program of China (2016YFA0602100).

**References**

Albrecht, B.: Aerosols, cloud microphysics, and fractional cloudiness, Science, 245, 1227–1230, 1989.

Adler, R. F., Chang, A.: The Version 2 Global Precipitation Climatology Project (GPCP) Monthly Precipitation Analysis (1979-Present), J. Hydrometeor., 4, 1147–1167, 2003

Alexander, M. J., May, P. T., and Beres, J. H.: Gravity waves generated by convection in the Darwin area during the Darwin Area Wave Experiment, J. Geophys. Res., 109, D20S04, doi: 10.1029/2004JD004729, 2004.

Allen, M., Stott, P., Mitchell, J., Schnur, R., and Delworth, T.: Quantifying the uncertainty in forecasts of anthropogenic climate change, Nature, 407, 617-620, 2000.

Arora, V. K., and Boer, G. J.: A parameterization of leaf phenology for the terrestrial ecosystem component of climate models, Global Change Biology, 11, 39-59, doi:10.1111/j.1365-2486.2004.00890.x, 2005.

Andreas, E. L.: A theory for the scalar roughness and the scalar transfer coefficients over snow and sea ice,

903 Bound.-Layer Meteor., 38, 159-184, 1987.
904 Andreas, E. L.: Parameterizing scalar transfer over snow and ice: A review, Journal of Hydrometeorology, 3,
905 417-432, 2002.
906 Andreas, E. L., Horst, T. W., Grachev, A. A., Persson, P. O. G., Fairall, C. W., and Guest, P. S.,and Jordan, R.E.:
907 Parametrizing turbulent exchange over summer sea ice and the marginal ice zone, Quartely Journal of the
908 Royal Meteorological Society, 136, 927-943, 2010a.
909 Andreas, E. L., Persson, P. G., Jordan, R. E., Horst, T.W., Guest, T.S., Grachev, A.A., and Fairall, C.W.:
910 Parameterizing turbulent exchange over sea ice in winter, Journal of Hydrometeorology, 11, 87-104, 2010b.
911 Andrews, T., Gregory, J. M., Webb, M. J., and, K. E.: Forcing, feedbacks and climate sensitivity in CMIP5
912 coupled atmosphereocean climate models, Geophys. Res. Lett, 38, L09712, doi: 10.1029/2012GL051607,
913 2012.
914 Beres, J. H., Alexander, M. J., and Holton, J. R.: A method of specifying the gravity wave spectrum above
915 convection based on latent heating properties and background wind, J. Atmos. Sci., 61, 324-337, 2004.
916 Boucher, O., Lohmann, U.: The sulphate-CCN-cloud albedo effect – a sensitivity study with two general
917 circulation models, Tellus 47B, 281–300, 1995.
918 Caesar, L., Rahmstorf, S., Robinson, A., Feulner, G., Saba, V.: Observed fingerprint of a weakening Atlantic
919 Ocean overturning circulation, Nature, 556, 191-196, 2018.
920 Campin J.M., and Goosse, H.: Parameterization of density-driven downsloping flow for a coarse-resolution ocean
921 model in z-coordinate, Tellus, 51A, 412–430, 1999.
922 Cao M., and Woodward F. I.: Net primary and ecosystem production and carbon stocks of terrestrial ecosystems
923 and their responses to climate change, Global Change Biology, 4, 185-198, 1998.
924 Chen C., and Cotton, W. R.: The physics of the marine stratocumulus-capped mixed layer, J. Atmos. Sci., 44 (50),
925 2951–2977, 1987.
926 Chen A., Li, W. P., Li, W. J., and Liu, X.: An observational study of snow aging and the seasonal variation of
927 snow albedo by using data from Col de Porte, France. Chinese Science Bulletin, 59 (34), 4881-4889, 2014
928 Collins, W. D., Rasch, P.J., Boville, B.A., Hack, J. J., McCaa, J.R., Williamson, D. L., Kiehl, J. T., Briegleb, B.,
929 Bitz C., Lin S.J., Zhang, M.H., and Dai, Y.J.: Description of the NCAR community atmosphere model
930 (CAM3). Technical Report NCAR/TN-464 + STR, National Center for Atmospheric Research, Boulder,
931 Colorado, 226 pp, 2004.
932 Collins, W. J., Lamarque, J.–F., Schulz,M., Boucher, O., Eyring, V., Hegglin, M. I., Maycock, A., Myhre, G.,

933 Prather, M., Shindell, D., and Smith, S. J.: AerChemMIP: quantifying the effects of chemistry and aerosols
934 in CMIP6, Geosci. Model Dev., 10, 585–607, 2017.
935 Danabasoglu, G., and Co-authors: North Atlantic simulations in Coordinated Ocean-ice Reference
936 Experiments phase II (CORE-II). Part I: Mean States. Ocean Modelling, 73, 76-107, doi:
937 10.1016/j.ocemod.2013.10.005, 2014.
938 Dee, D.P., Uppala, S. M., Simmons, A. J., Berrisford, P., Poli, P., Kobayashi, S., Andrae, U., Balmaseda, M. A.,
939 Balsamo, G., Bauer, P., Bechtold, P., Beljaars, A. C. M., Berg L., Bidlot, J., Bormann, N., Delsol, C., Dragani,
940 R., Fuentes, M., Geer, A. J., Haimberger, L., Healy, S. B., Hersbach, H., Holm, E. V., Isaksen, L., Kallberg, P.,
941 Kohler, M., Matricardi, M., NcNally, A.P., Monge-Sanz, B. M., Morcrette, J.-J., Park, B.-K., Peubey, C.,
942 Rosnay, P., Tavolato, C., Thepaut, J.-N., and Vitart F.: The ERA-Interim reanalysis: configuration and
943 performance of the data assimilation system,Quart. J. R. Meteorol. Soc., 137, 553-597 (DOI:
944 10.1002/qj.828) , 2011。
945 Ding, Y. H., Liu, Y. M., Song, Y. J., Li, Q. Q.: Research and experiments of the dynamical model system for
946 short-term climate prediction, Climatic Environ. Res., 7(2), 236–246, 2002 (in Chinese).
947 Eyring, V., Bony, S., Meehl, G. A., Senior, C. A., Stevens, B., Stouffer, R. J., Taylor, K. E.: Overview of the
948 Coupled Model Intercomparison Project Phase 6 (CMIP6) experimental design and organization, Geosci.
949 Model Dev., 9, 1937–1958, 2016, 2017.
950 Fetterer, F., Knowles, K., Meier, W., Savoie, M.: Sea Ice Index, digital media, National Snow and Ice Data Center.
951 Boulder, CO., 2002.
952 Fyfe, J.C., Meehl, G.A., England, M.H., Mann, M. E. Santer, B. D., Flato, G. M., Hawkins, E., Gillett, N. P., Xie,
953 S.–P., Kosaka, Y., Swart, N. C.: Making sense of the early-2000s warming slowdown, Nat. Clim. Change 6,
954 224–228, 2016.
955 Griffies, S. M., Gnanadesikan, A., Dixon, K. W., Dunn e, J. P., Gerdes, R., Harrison, M. J., Rosati, A., Lin, J.,
956 Bonita, R., Samuels, L., Spelman, M. J., Winton, M., Zhang, R.J.: Formulation of an ocean model for
957 global climate simulations, Ocean Sci., 1, 45–79, 2005.
958 Gregory, J. M., Ingram, W. J., Palmer, M. A., Jones, G. S., Stott, P. A., Thorpe, R. B., Lowe, J. A., Johns, T. C.,
959 and Williams, K. D.: A new method for diagnosing radiative forcing and climate sensitivity, Geophys. Res.
960 Lett., 31, L03205, doi:10.1029/2003GL018747, 2004.
961 Gregory, J.M., Webb, M. J., and Taylor, K. E.: Forcing, feedbacks and climate sensitivity in CMIP5 coupled
962 atmosphere-ocean climate models, Geophys. Res. Lett., 39, L09712, doi:10.1029/2012GL051607, 2012.

963 Gent, P. R., Mcwilliams, J. C.: Isopycnal mixing in ocean circulation Models[J]. Journal of Physical
964 Oceanography, 20(1), 150–155, 1990.
965 Guenther, A. B., Jiang, X., Heald, C. L., Sakulyanontvittaya, T., Duhl, T., Emmons, L. K., and Wang, X.: The
966 Model of Emissions of Gases and Aerosols from Nature Version 2.1 (MEGAN2.1): An Extended and
967 Updated Framework for Modeling Biogenic Emissions, Geoscientific Model Development 5(6): 1471–1492,
968 2012.
969 Hack, J. J., Parameterization of moist convection in the National Center for Atmospheric Research Community
970 Climate Model (CCM2), J. Geophys. Res., 99, 5551–5568, 1994.
971 Haarsma, R. J., Roberts, M. J., Vidale, P. L., Senior, C. A., Bellucci, A., Bao, Q., Chang, P., Corti, S., Fuckar, N.
972 S., Guemas, V., Hardenberg, J. von, Hazeleger, W., Kodama, C., Koenigk, T., Leung, L. R., Lu, J., Luo, J. –J.,
973 Mao, J., Mizielinski, M. S., Mizuta, R. Nobre, P., Satoh, M., Scoccimarro, E., Semmler, T., Small, J., and
974 Storch, J.–S. von : High Resolution Model Intercomparison Project (HighResMIP v1.0) for CMIP6, Geosci.
975 Model Dev., 9, 4185–4208, doi:10.5194/gmd-9-4185-2016, 2016.
976 Holtslag, A. A. M., and Boville, B. A.: Local versus nonlocal boundary-layer diffusion in a global climate model,
977 J. Climate, 6, 1825–1842, 1993.
978 Huffman, G., Bolvin, D., Braithwaite, D., Hsu, K., Joyce, R., Xie, P.: Integrated Multi-satellitE Retrievals for
979 GPM (IMERG), version 4.4. NASA's Precipitation Processing Center, accessed 31 March, 2015,
980 ftp://arthurhou.pps.eosdis.nasa.gov/gpmdata/, 2014.
981 IPCC Climate Change: The Physical Science Basis (eds Stocker, T. F., Qin, D., Plattner, G.-K., Tignor, M., Allen,
982 S. K., Boschung, J., Nauels, A., Xia, Y., Bex V., and Midgley, P. M.) , Cambridge Univ. Press, Cambridge,
983 United Kingdom and New York, NY, USA, 2013.
984 Ji, J.: A climate-vegetation interaction model: Simulating physical and biological processes at the surface, Journal
985 of Biogeography, 22, 2063-2069, 1995.
986 Ji, J., Huang, M., and Li, K.: Prediction of carbon exchange between China terrestrial ecosystem and atmosphere
987 in 21st century, Sci. China Ser. D: Earth Sci., 51(6), 885-898, 2008.
988 Li, J. D., Wang, W.-C., Liao, H., and Chang, W. Y.: Past and future direct radiative forcing of nitrate aerosol in
989 East Asia, Theoretical and Applied Climatology, 121, 445-458, 2015.
990 Lu, B., Ren, H.-L.: Improving ENSO periodicity simulation by adjusting cumulus entrainment in BCC_CSMs,
991 Dynamics of Atmospheres and Oceans, 76, 127-140, 2016.
992 Jiang X., Waliser, D. E.Xavier, P.K., Petch, J., Klingaman, N. P., Woolnough, S.J., Guan, B., Bellon, G., Crueger,

T., DeMott, C., Hannay, C., Lin, H., Hu, W., Kim, D., Lappen, C., Lu, M.–M., Ma, H.-Y., Miyakawa, T., Ridout, J. A., Schubert, S.D., Scinocca, J., Seo, K.-H., Shindo, E., Song, X., Stan, C., Tseng, W.-L., Wang, W., Wu, T., Wyser, K., Wu, X., Zhang, G. J., Zhu, H.: Exploring Key Processes of the Madden-Julian Oscillation (MJO): A Joint WGNE MJO Task Force / GEWEX GASS Project on the Vertical Structure and Diabatic Processes of the MJO – Part I. Climate Simulations, J. Geophys. Res. Atmos., 120, 4718–4748. doi:10.1002/2014JD022375, 2015.

Jin, X., Wu, T., Li, L.: The quasi-stationary feature of nocturnal precipitation in the Sichuan Basin and the role of the Tibetan Plateau, Climate Dynamics, 41: 977-994. DOI: 10.1007/s00382-012-1521-y, 2013.

Jones, C.D., Arora, V., Friedlingstein, P., Bopp, L., Brovkin, V., Dunne, J., Graven, H., Hoffman, F., Ilyina, T., John, J. G., Jung, M., Kawamiya, M., Koven, C., Pongratz, J., Raddatz, T., Randerson, J. T., and Zaehle, S.: C4MIP – The Coupled Climate–Carbon Cycle Model Intercomparison Project: experimental protocol for CMIP6, Geosci. Model Dev., 9, 2853–2880, doi:10.5194/gmd-9-2853-2016, 2016.

Klein, S. A., and Hartmann, D. L.: The seasonal cycle of low stratiform clouds, J. Climate, 6, 1587–1606, 1993.

Kristjánsson, J. E., Edwards, J. M., Mitchell, D. L.: Impact of a new scheme for optical properties of ice crystals on climates of two GCMs, J. Geophys. Res., 105(D8), 10063–10079, doi:10.1029/2000JD900015, 2000.~~Kristjánsson, J. E., and Kristiansen, J.: Impact of a new scheme for optical properties of ice crystals on climates of two gcms, J. Geophys. Res., 105, 10063–10079, 2000.~~

Lamarque, J.-F., Emmons, L. K., Hess, P. G., Kinnison, D. E., Tilmes, S., Vitt, F., Heald, C. L., Holland, E. A., Lauritzen, P. H., Neu, J., Orlando, J. J., Rasch, P. J., and Tyndall, G. K.: CAM-chem: description and evaluation of interactive atmospheric chemistry in the Community Earth System Model, Geosci Model Dev, 5, 369-411, 2012.

Large, W. G., McWilliams, J. C., and Doney, S. C.: Oceanic vertical mixing: A review and a model with a nonlocal boundary layer parameterization, Rev. Geophys., 32, 363-403, 1994.

Liu, Y., and Daum, P. H.: Indirect warming effect from dispersion forcing, Nature, 419, 580-581, 2002.

Liou, K. N.: An Introduction to Atmospheric Radiation, China Meteorological Press, 313-327 (in Chinese), 2004.

Loeb, N.G., Lyman, J.M., Johnson, G.C,, Allan, R.P., Doelling, D.R., Wong, T., Soden, B.J., and Stephens, G.L.: Observed changes in top-of-the-atmosphere radiation and upper-ocean heating consistent within uncertainty, Nature Geosciences, DOI 10.1038/NGE, 2012.

Lu, Y., Zhou, M., and Wu, T.: Validation of parameterizations for the surface turbulent fluxes over sea ice with CHINARE 2010 and SHEBA data, Polar Research, 32, 20818, http://dx.doi.org/10.3402/polar.v32i0.20818,

2013.

Meehl, G.A., Boer, G.J., Covey, C., Latif, M., Stouffer, R.J.: Intercomparison makes for a better climate model. Eos, Trans.Amer.Geophys.Union, 78, 445--451, doi:10.1029/97EO00276.

Medhaug, I., Martin, B. S., Erich, M. F., and Knutti, R.: Reconciling controversies about the 'global warming hiatus', Nature, 545, 41–47, 2017.

Morice, C, P., Kennedy, J. J., Rayner, N.A., and Jones, P.D.: Quantifying uncertainties in global and regional temperature change using an ensemble of observational estimates: The HadCRUT4 data set, J. Geophys. Res. 117, D08101, 2012.

Martin, G.M., Johnson, D.W., and Spice, A.: The measurement and parameterisation of effective radius of droplets in warm stratocumulus clouds, J. Atmos. Sci., 51, 1823–1842, 1994.

McFarlane, N. A.: The effect of orographically excited gravity wave drag on the general circulation of the lower stratosphere and troposphere, J. Atmos. Sci., 44, 1775-1800, 1987.

Oleson, K. W., Lawrence, D. M. and Dai, Y. J.: Technical description of the Community Land Model (CLM), NCAR Technical Note NCAR/TN-461+STR, 2004.

Pontikis, C.A., and Hicks, E.; Contribution to the cloud droplet effective radius parameterization, Geophys. Res. Lett. 19, 2227–2230, 1992.

Peng, Y., and Lohmann, U.: Sensitivity study of the spectral dispersion of the cloud droplet size distribution on the indirect aerosol effect, Geophys. Res. Lett., 30(10), 1507, doi:10.1029/2003GL017192, 2003.

Quaas J, Boucher O, and Lohmann U: Constraining the total aerosol indirect effect in the LMDZ and ECHAM4 GCMs using MODIS satellite data. Atmos Chem Phys 6,947-955, 2006

Rasch, P. J., and Kristj ánsson, J. E.: A comparison of the CCM3 model climate using diagnosed and predicted condensate parameterizations, J. Climate, 11, 1587-1614, 1998.

Rahmstorf, S.: A fast and complete convection scheme for ocean models, Ocean Modelling, 101, 9–11, 1993.

Rayner, N. A., Parker, D. E., Horton, E. B., Folland, C., Alexander, L., Rowell, D., Kent, E., and Kaplan, A.: Global analyses of sea surface temperature, sea ice, and night marine air temperature since the late nineteenth century, Journal of Geophysical Research, 108(D14), 4407, doi:10.1029/2002JD002670, 2003.

Richter, J. H., Sassi, F., and Garcia, R. R.: Toward a physically based gravity wave source parameterization in a general circulation model, J. Atmos. Sci., 67, 136--156, 2010.

Sweeney, C., Gnanadesikan, A., Griffies, S. M., Harrison, M., Rosati, A., Samuels, B.: Impacts of shortwave penetration depth on large-scale ocean circulation and heat transport, Journal of Physical Oceanography 35,

1103–1119, 2005.

Stevens, B., Fiedler, S., Kinne, S., Peters, K., Rast, S., Musse, J., Smith, S.J., and Mauritsen, T.: MACv2-SP: a parameterization of anthropogenic aerosol optical properties and an associated Twomey effect for use in CMIP6, Geos.Mod.Dev.,10, 433-452, 2017.

Talley, L.D.; Closure of the global overturning circulation through the Indian, Pacific, and Southern Oceans: Schematics and transports, Oceanography, 26, 80–97, 2013.

Tan, H.H., Zhang, L.J., Chu, M., Wu, T.W., Qiu, B., and Li, J.L.: An analysis of simulated global sea ice extent, thickness, and causes of error with the BCC_CSM model. Chinese Journal of Atmospheric Sciences (in Chinese), 39 (1): 197−209, 2015.

Taylor, K. E., Stouffer, R. J., and Meehl, G. A.: An Overview of Cmip5 and the Experiment Design, B. Am. Meteorol. Soc., 93, 485–498, 2012.

Tietsche, S., Balmaseda, M., Zuo, H., Mogensen, K.: Arctic sea ice in the ECMWF MyOcean2 ocean reanalysis ORAP5. Tech Rep 737, European Center for Medium-Range Weather Forecasts, Reading, UK, 2014.

Wielicki, B.A., Barkstrom, B. R., Harrison, E. F., Lee, R. B., Smith, G. L., and Cooper, J. E.: Clouds and the earth's radiant energy system (CERES): an earth observing system experiment, Bull. Am. Meteorol. Soc., 77, 853–868, 1996.

Winton, M.: A reformulated three-layer sea ice model, J. Atmo.Oceanic Technol., 17, 525–531, 2000.

Wu, T., Song, L., Li, W., Wang, Z., Zhang, H., Xin, X., Zhang, Y., Zhang, L., Li, J., Wu, F., Liu, Y., Zhang, F., Shi, X., Chu, M., Zhang, J., Fang, Y., Wang, F., Lu,Y., Liu, X., Wei, M., Liu, Q., Zhou, W., Dong, M., Zhao, Q., Ji, J., Li, L., and Zhou, M.: An overview of BCC climate system model development and application for climate change studies, J. Meteor. Res., 28(1), 34-56, 2014.

Wu, T., Li, W., Ji, J., Xin, X., Li, L., Wang, Z., Zhang, Y., Li, J., Zhang, F., Wei, M., Shi, X., Wu, F., Zhang, L., Chu, M., Jie, W., Liu, Y.,Wang, F., Liu, X., Li, Q., Dong, M., Liang, X., Gao, Y., and Zhang, J.: Global carbon budgets simulated by the Beijing climate center climate system model for the last century, J Geophys Res Atmos, 118, 4326-4347. doi: 10.1002/jgrd.50320, 2013.

Wu, T.: A Mass-Flux Cumulus Parameterization Scheme for Large-scale Models: Description and Test with Observations, Clim. Dyn., 38:725–744, DOI: 10.1007/ s00382-011-0995-3, 2012.

Wu, T., Yu, R., Zhang, F., Wang, Z., Dong, M., Wang, L., Jin, X., Chen, D.L., and Li, L.: The Beijing Climate Center atmospheric general circulation model: description and its performance for the present-day climate, Climate Dynamics, 34, 123-147, DOI 10.1007/s00382-008-0487-2, 2010.

带格式的: 字体: (默认) Times New Roman, 11 磅, 字体颜色: 文字 1, 图案: 清除

带格式的: 字体: (默认) Times New Roman, 11 磅, 字体颜色: 文字 1, 图案: 清除

带格式的: 字体: (默认) Times New Roman, 11 磅, 字体颜色: 文字 1, 图案: 清除

Wu, T., Yu, R., and Zhang, F.: A modified dynamic framework for atmospheric spectral model and its application, J. Atmos.Sci., 65, 2235-2253, 2008

Wu, T., and Wu, G.: An empirical formula to compute snow cover fraction in GCMs, Adv.Atmos.Sci., 21, 529-535, 2004.

Xia, K., Luo, Y., and Li, W. P.: Simulation of freezing and melting of soil on the northeast Tibetan Plateau. Chinese Sci. Bull., 56, 1-4, doi: 10.1007/s11434-011-4542-8, 2011.

Xin, X., Wu, T., and Zhang, J.: Introduction of CMIP5 experiments carried out with the climate system models of Beijing Climate Center, Adv. Clim. Change Res., 4(1), 41-49，doi: 10.3724/SP.J.1248.2013.041, 2013.

Xu, K. M., and Krueger, S. K.: Evaluation of cloudiness parameterizations using a cumulus ensemble model, Mon. Wea. Rev., 119, 342–367, 1991.

Xu, L., and Penner, J.E.: Global simulations of nitrate and ammonium aerosols and their radiative effects, Atmos. Chem. Phys., 12, 9479-9504, 2012.

Zeng, X., Zhao, M., and Dickinson, R. E.: Intercomparison of bulk aerodynamic algorithms for the computation of sea surface fluxes using TOGA COARE and TAO data, J. Climate, 11, 2628-2644, 1998.

Zeng, X., Zhang, Q., Johnson, D., and Tao, W.-K.: Parameterization of wind gustiness for the computation of ocean surface fluxes at different spatial scales, Monthly Weather Review, 130, 2125-2133, 2002.

Zhang, G.J.: Convective quasi-equilibrium in midlatitude continental environment and its effect on convective parameterization. J Geophys Res 107(D14), doi:10.1029/2001JD001005, 2002.

Zhang, M., Lin, W., Bretherton, C. S., Hack, J. J., and Rasch, P. J.: A modified formulation of fractional stratiform condensation rate in the NCAR community atmospheric model CAM2, J. Geophys. Res., 108 (D1), 2003.

Zhang, Y., Gao, Z., Li, D., Li, Y., Zhang, N., Zhao, X., and Chen, J.: On the computation of planetary boundary-layer height using the bulk Richardson number method, Geosci. Model Dev., 7, 2599–2611, 2014.

Zhou, W.Y., Luo, Y., Li, W.P., Shi, X.L., and Zhang, Y: Comparative studies of different radiation schemes within vegetation in land model, Chinese Science Bulletin, 63, 10.1360/N972018-00398, 2018.

Table 1. BCC models for CMIP5 and CMIP6

| Model versions | Atmosphere | Atmos Chemistry and Aerosol | Land Surface | Ocean | Sea Ice |
|---|---|---|---|---|---|
| BCC-CSM1.1 in CMIP5 (Wu et al., 2013) | BCC-AGCM2.1<br>(1) T42，26 layers<br>(2) Top at 2.917 hPa | (1) Prescribed aerosols<br>(2) No atmospheric chemistry<br>(3) Global carbon budget without spatial distribution | BCC-AVIM1.0 | MOM4-L40v1<br>(1) Tri-polar: 0.3 to 1 deg latitude x 1 deg longitude, and 40 layers<br>(2) Oceanic carbon cycle based on OCMIP2 | SISv1 |
| BCC-CSM1.1m in CMIP5 (Wu et al., 2013) | BCC-AGCM2.2<br>(1) T106，26 layers<br>(2) Top at 2.917 hPa | Same as BCC-CSM1.1 | BCC-AVIM1.0 | MOM4-L40v2 | SISv2 |
| BCC-CSM2-MR In CMIP6 | BCC-AGCM3-MR<br>(1) T106，46 layers<br>(2) Top at 1.459 hPa | (1) Prescribed aerosols<br>(2) No atmospheric chemistry<br>(3) Prognostic spatial $CO_2$ in the atmosphere | BCC-AVIM2.0 | MOM4-L40v2 | SISv2 |
| BCC-CSM2-HR In CMIP6 | BCC-AGCM3-HR<br>(1) T266，56 layers<br>(2) Top at 0.092 hPa | (1) Prescribed aerosols<br>(2) No atmospheric chemistry | BCC-AVIM2.0 | MOM4-L40v2 | SISv2 |
| BCC-ESM1 In CMIP6 | BCC-AGCM3-Chem<br>(1) T42，26 layers<br>(2) Top at 2.917 hPa | (1) Prognostic aerosols<br>(2) MOZART2 atmospheric chemistry | BCC-AVIM2.0 | MOM4-L40v2 | SISv2 |

Table 2. Main physics schemes in atmospheric components (BCC-AGCM) of BCC-CSM versions for CMIP5 and CMIP6

| | **BCC-AGCM2 for CMIP5** | **BCC-AGCM3 for CMIP6** |
|---|---|---|
| **Deep convection** | The cumulus convection parameterization scheme (Wu, 2012) | A modified Wu'2012 scheme described in this work |
| **Shallow/Middle Tropospheric Moist Convection** | Hack (1994) | Hack (1994) |
| **Cloud macrophysics** | Cloud fraction diagnosed from updraft mass flux and relative humidity (Collins et al., 2004) | A new scheme to diagnose cloud fraction described in this work |
| **Cloud microphysics** | Modified scheme of Rasch and Kristj ánsson (1998) by Zhang et al. (2003).<br>No aerosol indirect effects | Modified scheme of Rasch and Kristj ánsson (1998) by Zhang et al. (2003), but included the aerosol indirect effects in which liquid cloud droplet number concentration is diagnosed using the aerosols masses. |
| **gravity wave drag** | Gravity wave drag only generated by orography (Mcfarlane 1987) | Gravity wave drag generated by both orography (Mcfarlane 1987) and convection (Beres et al., 2004) using tuned parameters related to model resolutions. |
| **Radiative transfer** | Radiative transfer scheme used in CAM3 (Collins et al., 2004) with no aerosol indirect effects, and cloud drop effective radius for clouds is only function of temperature and has a distinct difference between maritime, polar, and continental for warm clouds. | Radiative transfer scheme used in CAM3 (Collins et al., 2004), but including the aerosol indirect effects, and the effective radius of the cloud drop for liquid clouds is diagnosed using liquid cloud droplet number concentration. |
| **Boundary Layer** | ABL parameterization [Holtslag and Boville, 1993] | ABL parameterization [Holtslag and Boville, 1993], but modified PBL height computation referred to Zhang et al. (2014) |

Table 3. Main physics schemes in BCC-AVIM versions

| BCC-AVIM1.0 in CMIP5 | BCC-AVIM2.0 in CMIP6 |
|---|---|
| ◆ Soil-Vegetation-Atmosphere Transfer module<br>◆ Multi-layer snow-soil scheme (same as NCAR CLM3)<br>◆ Snow Cover Fraction scheme (sub-grid topography)<br>◆ Vegetation growth module<br>◆ Soil carbon decomposition module<br>◆ Land use change module (variable crop planting area) | ◆ Modified freeze-thaw scheme for soil water (below 0 degree and dependent on soil & water) (Xia et al., 2011)<br>◆ Improved parameterization of snow surface albedo (Chen et al., 2014) and snow cover fraction (Wu and Wu, 2004)<br>◆ Four-stream radiation transfer through vegetation canopy (Zhou et al., 2018)<br>◆ A vegetation phenology similar to Canadian Terrestrial Ecosystem Model (Arora and Boer, 2005)<br>◆ Parameterized rice paddy scheme<br>◆ land VOC module (Guenther et al., 2012) |

**带格式的：**字体：（默认）+西文正文（Calibri）

Table 4. Energy balance and cloud radiative forcing at the top-of-atmosphere (TOA) in the model with contrast to CERES/EBAF and CERES observations. Units: W • –m$^{-2}$.

| | BCC-CSM2-MR (CMIP6) | BCC-CSM1.1m (CMIP5) | CERES/EBAF (OBS) | CERES (OBS) |
|---|---|---|---|---|
| Net energy at TOA | 0.85 | 0.98 | 0.81 | 5.73 |
| TOA outgoing longwave radiative flux | 239.15 | 236.10 | 239.72 | 238.95 |
| TOA incoming shortwave Radiation | 340.46 | 341.70 | 340.18 | 341.47 |
| TOA net shortwave radiative flux | 239.09 | 235.96 | 240.53 | 244.68 |
| TOA outgoing longwave radiative flux in clear sky | 265.02 | 265.58 | 265.80 | 266.87 |
| TOA net shortwave radiative flux in clear sky | 288.67 | 288.71 | 287.68 | 294.69 |
| Shortwave cloud radiative forcing | -49.55 | -52.71 | -47.16 | -48.58 |
| Longwave cloud radiative forcing | 25.87 | 29.48 | 26.07 | 27.19 |

Notes: The model data are the mean of 1986~~1~~ to 2005~~14~~, while the available observation data are for 2003–2014.

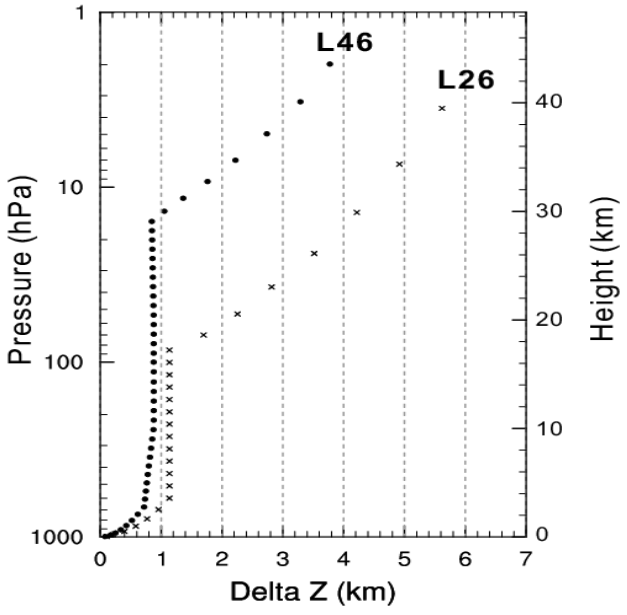


Figure 1. The profiles of layer thickness against the height for 26 vertical layers of the atmosphere in BCC-CSM-1.1m and 46 vertical layers in BCC-CSM2-MR.

带格式的：居中

带格式的：字体：（默认）Times New Roman，11 磅，字体颜色：黑色

带格式的：字体：（默认）Times New Roman

带格式的：字体：（默认）Times New Roman

带格式的：字体：（默认）Times New Roman

带格式的：定义网格后不调整右缩进，行距：1.5 倍行距，无孤行控制，不调整西文与中文之间的空格，不调整中文和数字之间的空格

带格式的：字体：（默认）Times New Roman，11 磅，字体颜色：黑色

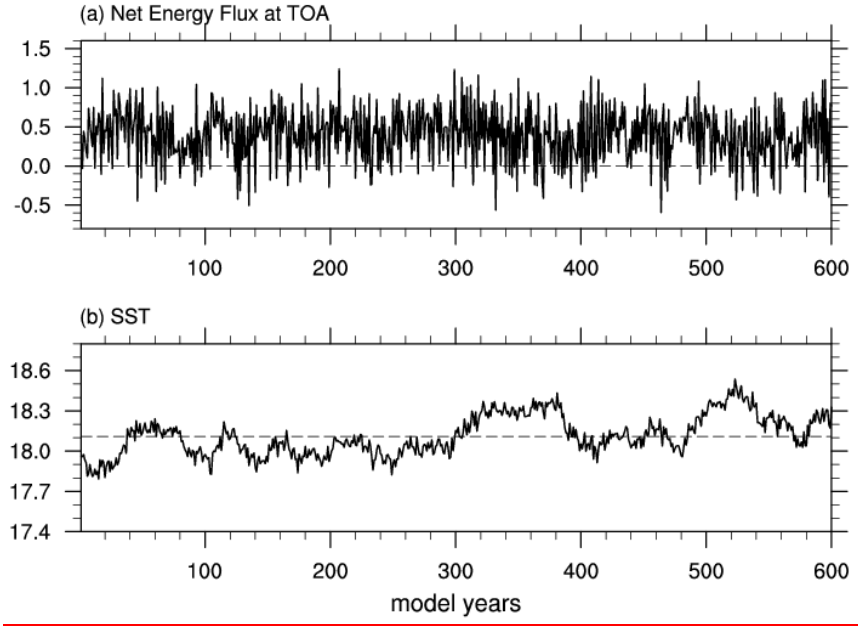


Figure 2. The time series of (a) global mean net energy flux at top of the atmosphere ($W \cdot m^{-2}$) and (b) global sea surface temperature for the 600 years of piControl simulations.

带格式的：居中

带格式的：行距：1.5 倍行距

带格式的：字体：（默认）Times New Roman

带格式的：上标

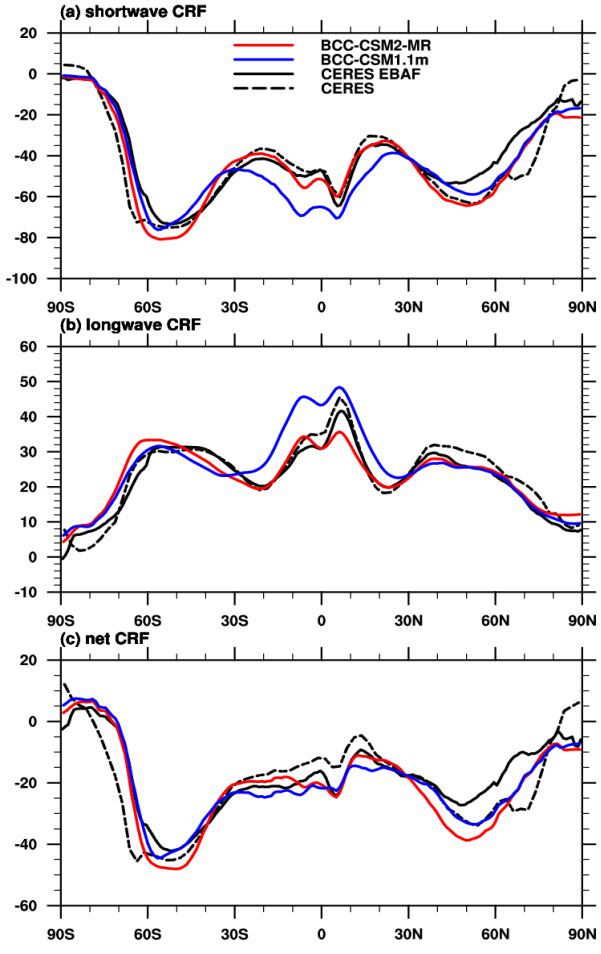


Figure 3~~1~~. Zonal averages of the cloud radiative forcing from the BCC CMIP5 and CMIP6 models and observations (in $W_{-}m^{-2}$; top row: shortwave effect; middle row: longwave effect; bottom row: net effect). Model results are for the period 198~~6~~5–2005, while the available CERES ES-4 and CERES EBAF 2.6 data set are for 2003–2014.

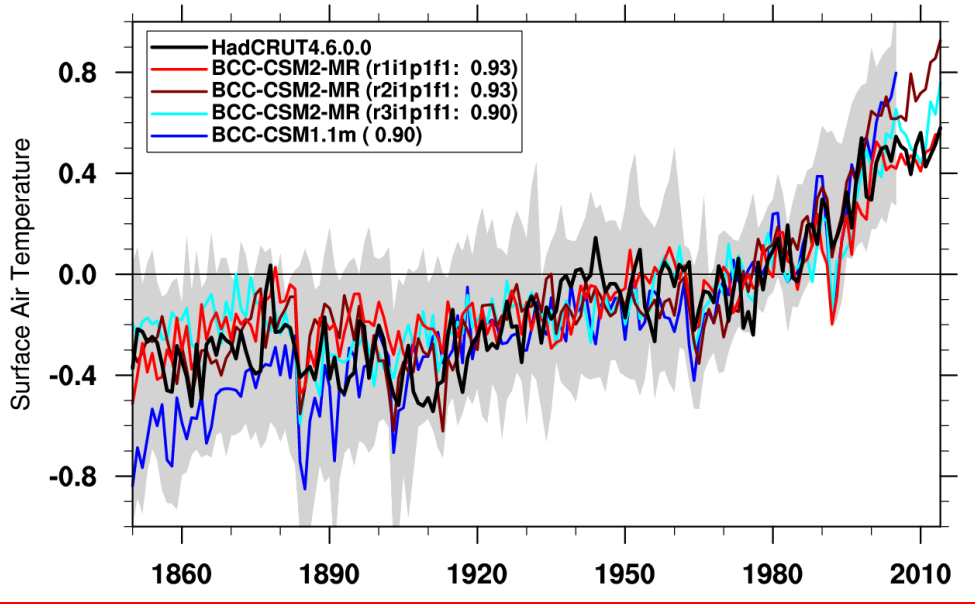


Figure 4. Time series of anomalies in the global (60 ℃S to 60 ℃N) mean surface air temperature from 1850 to 2014. The reference climate to deduce anomalies is for each individual curve from 1961 to 1990. Three lines labeled BCC-CSM2-MR denote three members of historical simulations from different initial state of the piControl simulation. The numbers in the bracket denote the correlation coefficient of 11-year smoothed BCC model data with the HadCRUT4.6.0.0 (Morice et al., 2012) observation. Gray shaded area shows the spread of 36 CMIP5 models data.

**带格式的：**定义网格后不调整右缩进，无孤行控制，不调整西文与中文之间的空格，不调整中文和数字之间的空格，制表位：不在 3.43 字符

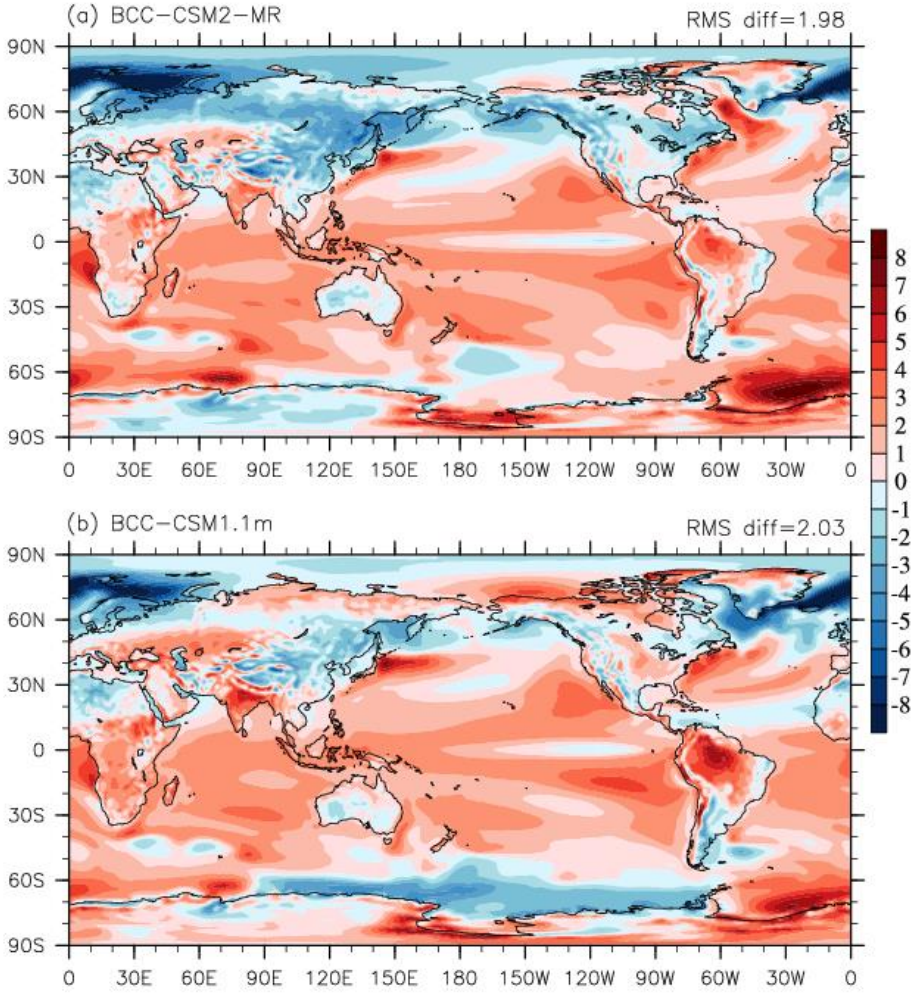


Figure 5~~2~~. Annual-mean surface (2 meter) air temperature biases (℃) of (a) BCC-CSM2-MR and (b) BCC-CSM1.1m simulations with contrast to the reanalysis ERA-Interim for the period of 1986 to 2005.

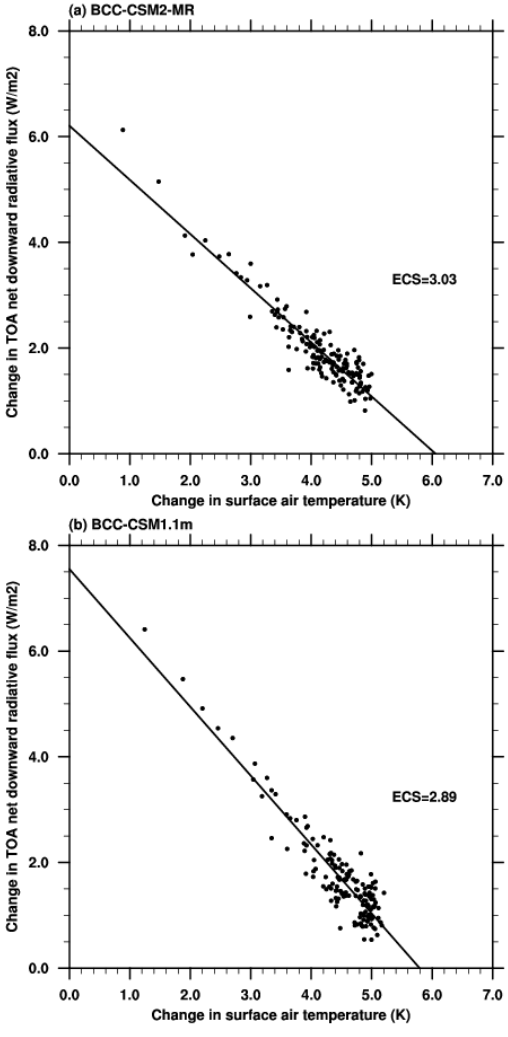


Figure 6. Relationships between the change in net top-of-atmosphere radiative flux and global-mean surface air temperature change simulated with an abrupt 4x$CO_2$ increase relative to the pre-industrial control run.

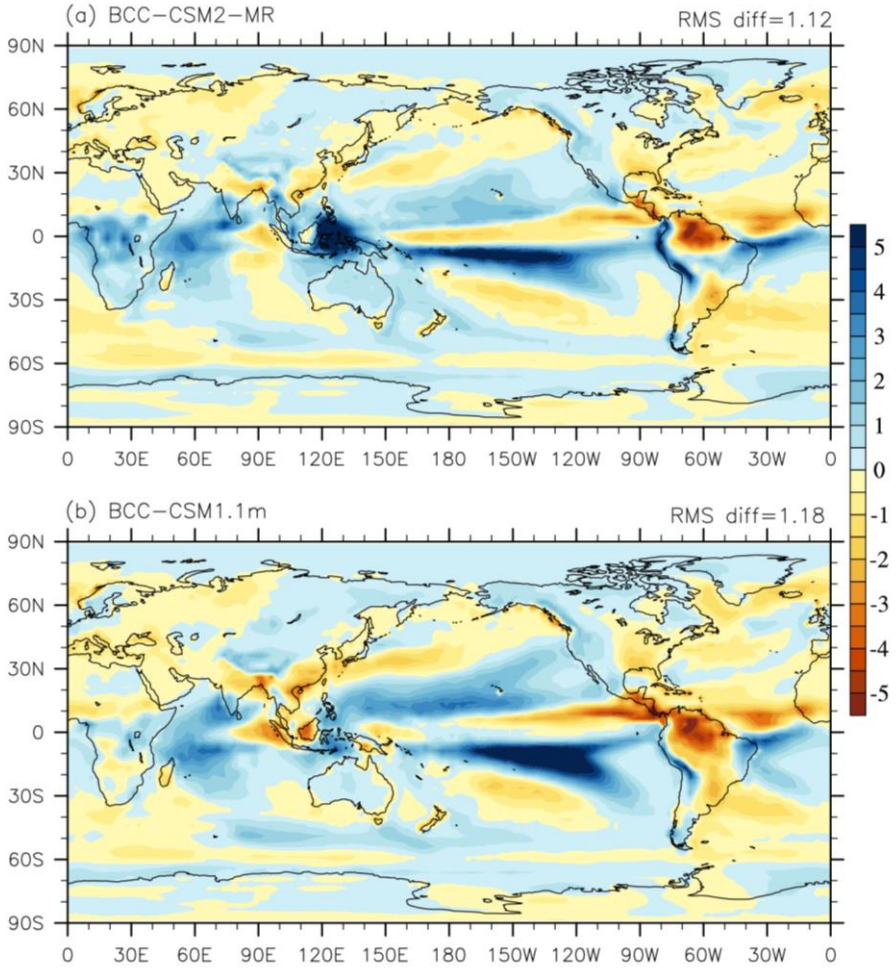


Figure 7~~3~~. ~~-~~ Annual-mean precipitation rate biases (mm ~~-~~day$^{-1}$) of (a) BCC-CSM2-MR and (b) BCC-CSM1.1m simulations with contrast to 1986-2005 precipitation analyses from the Global Precipitation Climatology Project (Adler et al., 2003)

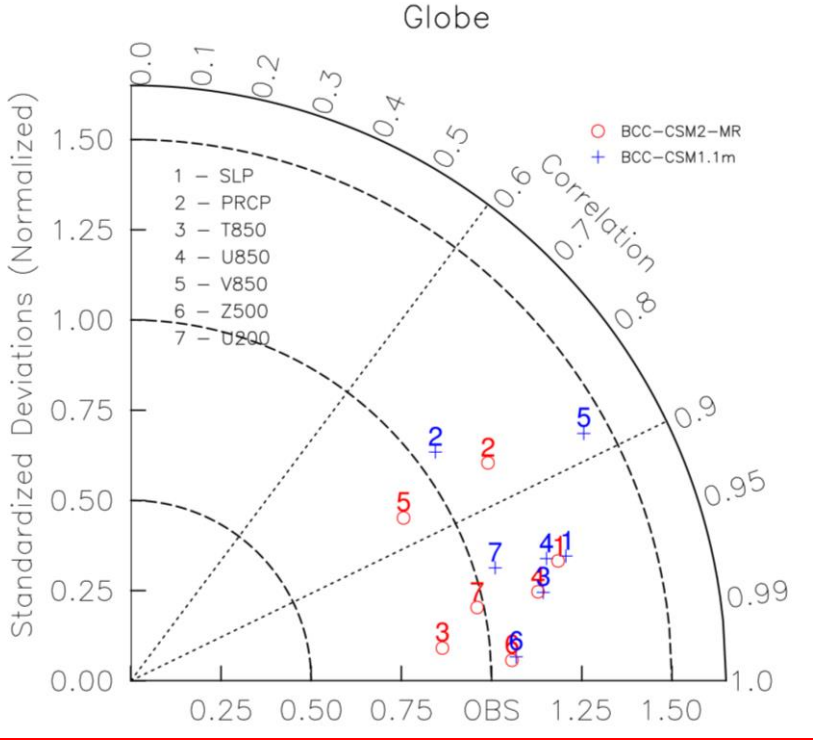
Globe
BCC–CSM2–MR
BCC–CSM1.1m
1 – SLP
2 – PRCP
3 – T850
4 – U850
5 – V850
6 – Z500
7 – U200
Correlation
Standardized Deviations (Normalized)
0.0
0.1
0.2
0.3
0.4
0.5
0.6
0.7
0.8
0.9
0.95
0.99
1.0
0.00
0.25
0.50
0.75
1.00
1.25
1.50
0.25
0.50
0.75
OBS
1.25
1.50

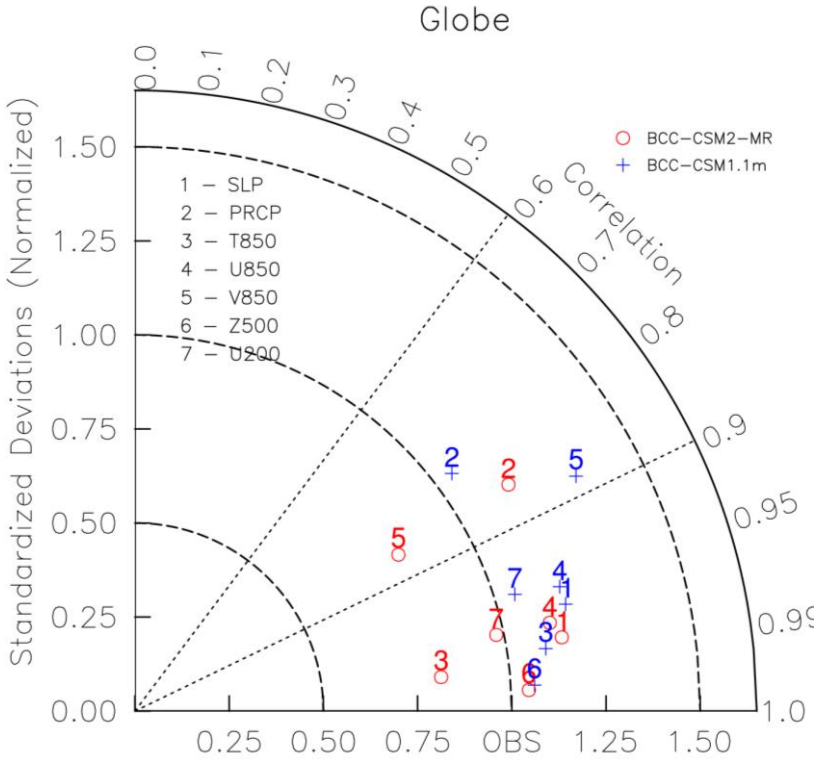


Figure 84. Taylor diagram for the global climatology (1980–2005) of sea level pressure (SLP), precipitation (PRCP), temperature at 850 hPa (T850), zonal wind at 850 hPa (U850), longitudinal wind at 850 hPa (V850), geopotential height at 500 hPa (Z500), and zonal wind at 200 hPa (U200). The radial coordinate shows the standard deviation of the spatial pattern, normalized by the observed standard deviation. The azimuthal variable shows the correlation of the modelled spatial pattern with the observed spatial pattern. Analysis is for the whole globe. The reference dataset is ERA-InterimNCEP except the precipitation from Global Precipitation Climatology Project dataset. The model results of BCC-CSM2-MR and BCC-CSM1.1m are the mean for 1980 to 2000. Blue crosses are for BCC-CSM1.1m and circles for BCC-CSM2-MR.

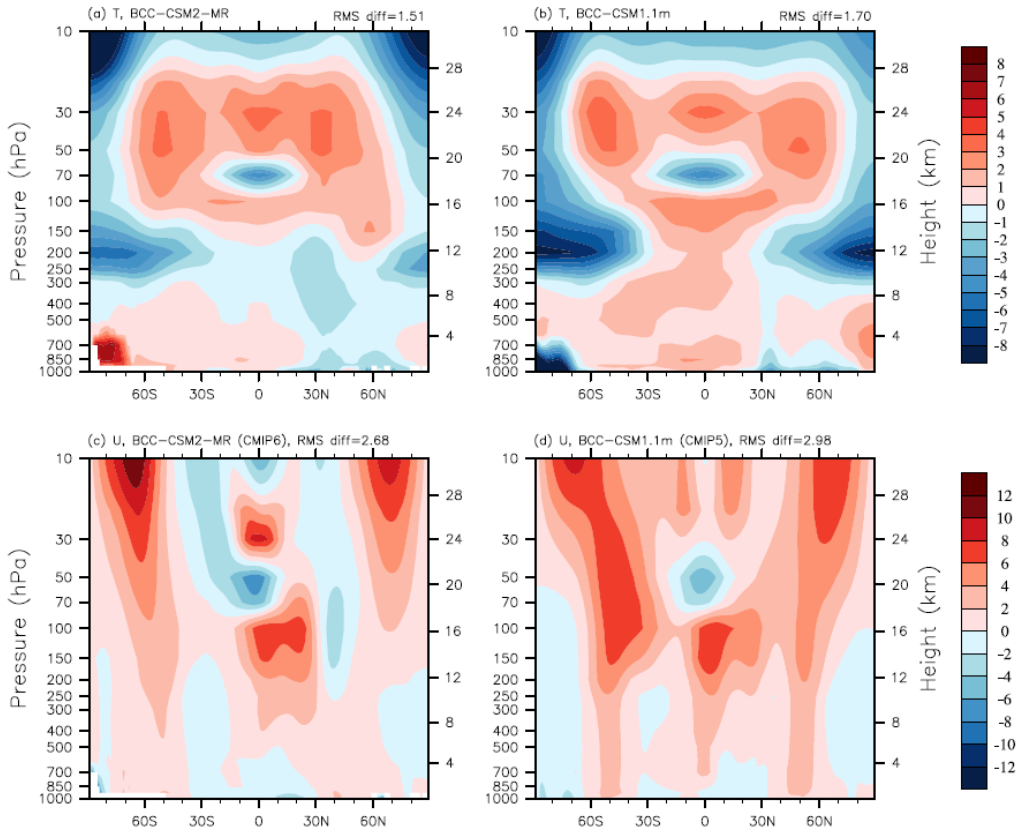


Figure 9~~5~~. Pressure-latitude sections of annual mean temperature (top panels, K) and zonal wind (bottom, m·s$^{-1}$) biases for BCC-CSM2-MR (left) and BCC-CSM1.1m (right), with respect to the reanalysis ERA-Interim for the period of 1986 to 2005.

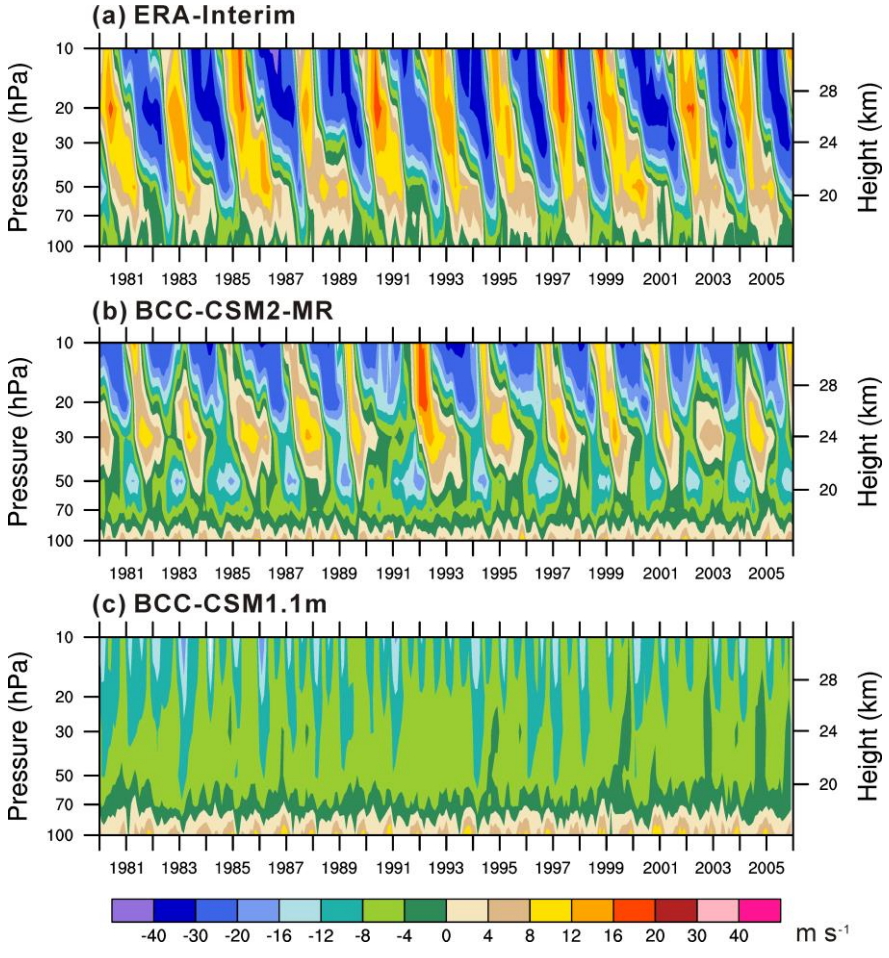


Figure 10~~6~~. Tropical zonal winds (m s$^{-1}$) between 5 ℃S and 5 ℃N in the lower stratosphere from 1980 to 2005 for (a) ERA-Interim reanalysis, (b) BCC-CSM2-MR, and (c) BCC-CSM1.1m.

带格式的：上标

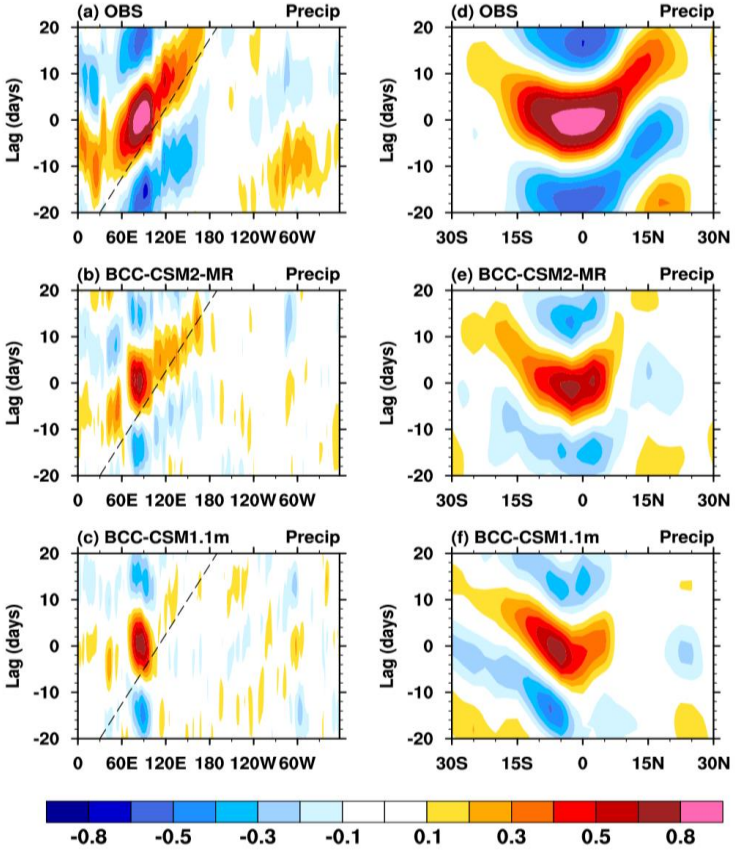


Figure 11~~7~~. Left panels: longitude-time evolution of lagged correlation coefficient for the 20–100 day band-pass-filtered anomalous rainfall (averaged over 10 °S–10 °N) against itself averaged over the equatorial eastern Indian Ocean (75 °–85 °E; 5 °S–5 °N). Right panels: same as in the left panels but to show meridional propagation of the filtered rainfalls, and lagged correlation coefficient for anomalous rainfall (averaged over 80 °–100 °E) against the rainfall averaged over the same region of equatorial eastern Indian Ocean.~~Right panels: same as in the left panels, but for latitude-time sections showing meridional propagation of the filtered rainfalls.~~ Dashed lines in each panel denote the 5 m ~~·~~s$^{-1}$ eastward propagation speed. The reference GPCP observations and historical simulations of models are ~~is~~ from the period of 1997-2005. ~~Models are from their historical simulations.~~

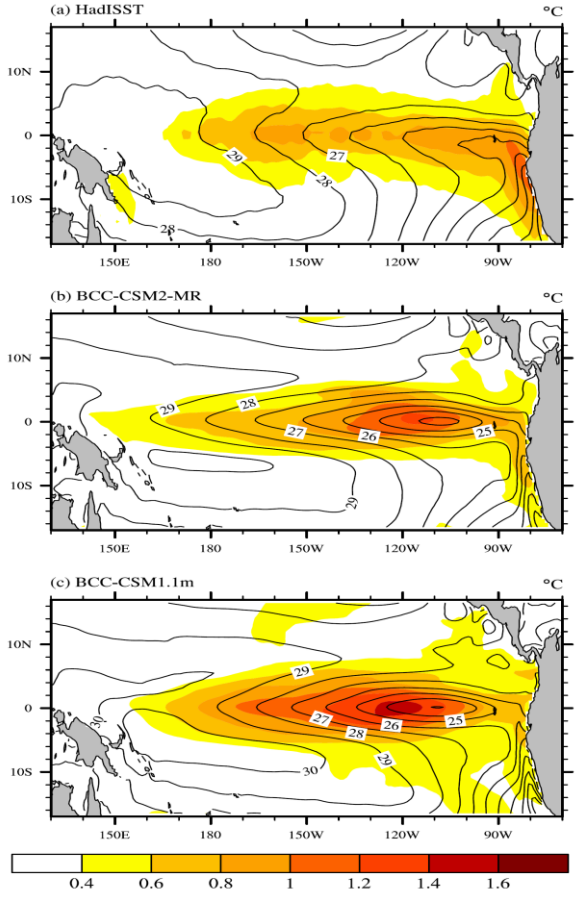


Figure 12~~9~~. The spatial distributions of 1986-2005 annual mean sea surface temperature (contour lines, ℃) and its standard deviation of interannual anomalies (shaded area, ℃) in the tropical Pacific for (a) HadISST observations (Rayner et al., 2003), (b) BCC-CSM2-MR, (c) BCC-CSM1.1m.

**带格式的：** 字体：（默认）Times New Roman，（中文）+中文正文（宋体）

**带格式的：** 字体：（默认）Times New Roman，（中文）+中文正文（宋体）

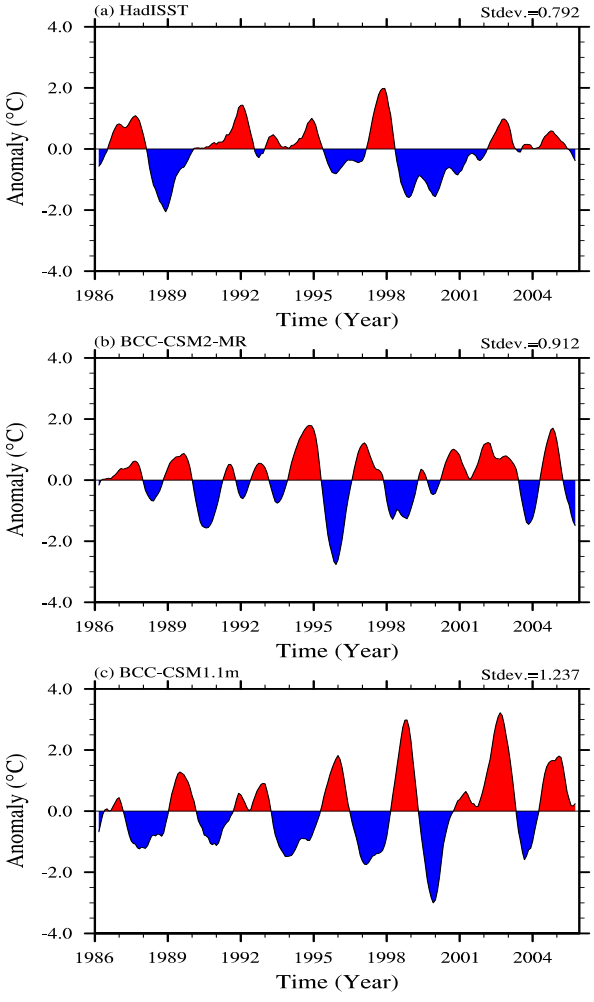


Figure 1~~3~~0. The time series of Nino3.4 SST Index from 1986 to 2005 for (a) HadISST data, (b) BCC-CSM2-MR, (c) BCC-CSM1.1m.

带格式的：孤行控制

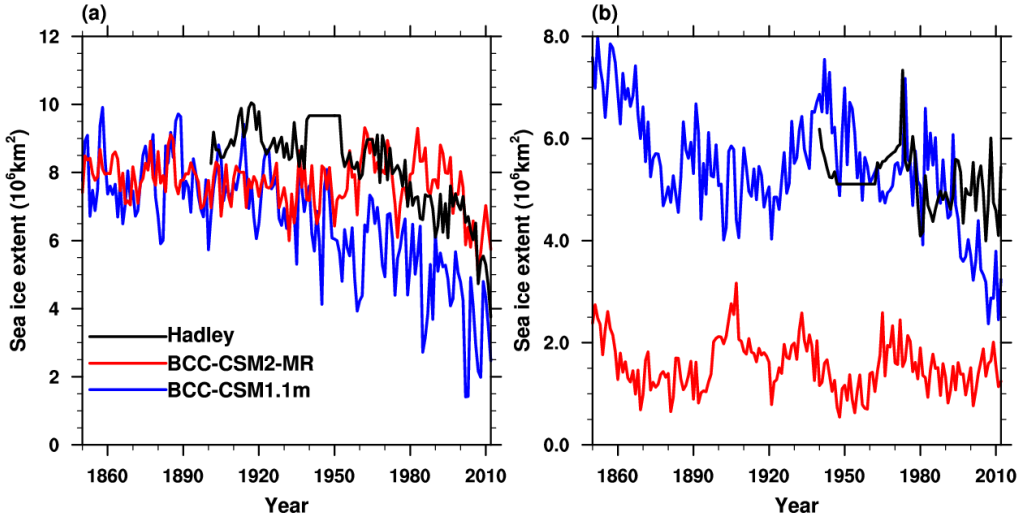


Figure 14. Time-series of sea-ice extent from 1851 to 2012 for (a) the Arctic in September and (b) the Antarctic in March as simulated in BCC-CSM2-MR and BCC-CSM1.1m and observations that are derived from Hadley Centre Sea Ice and Sea Surface Temperature data set (Rayner et al., 2003).

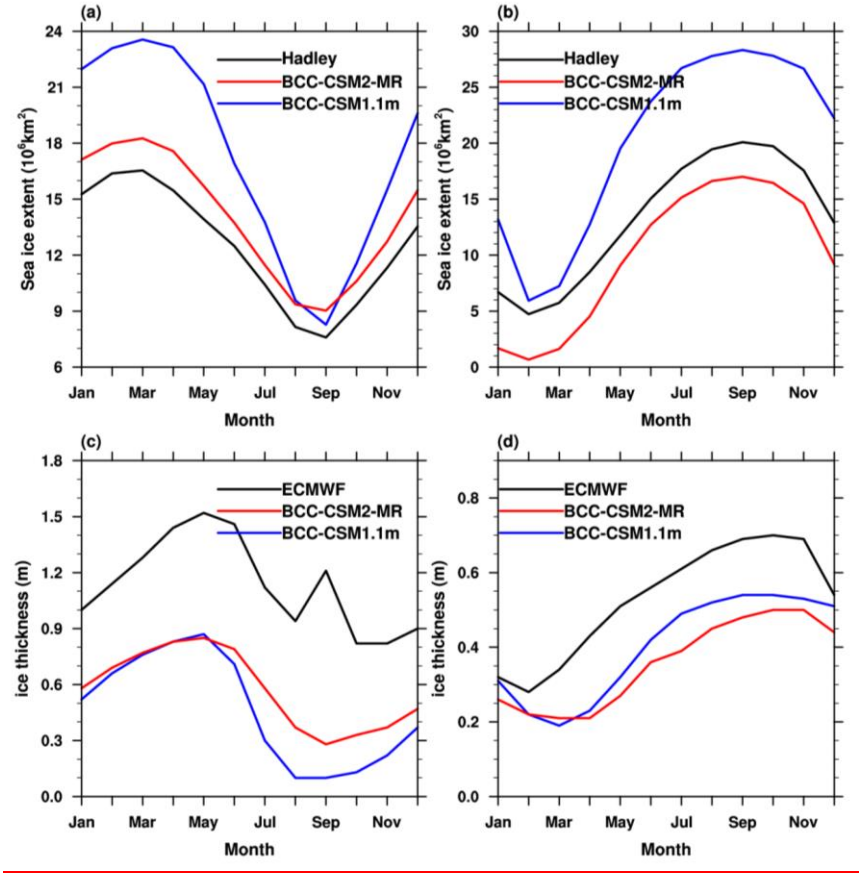


Figure 15~~8~~. Mean (1980–2005) seasonal cycle of sea-ice extent (upper panel, the ocean area with a sea-ice concentration of at least 15%) and mean thickness (lower panel) in the Northern Hemisphere (left) and the Southern Hemisphere (right). The observed seasonal cycles ~~(1980–2005)~~ of sea-ice extent in (a) and (b) are derived from 1980-2005 Hadley Centre Sea Ice and Sea Surface Temperature data set (Rayner et al., 2003), and ~~based on the National Snow and Ice Data Center (NSIDC; Fetterer et al., 2002) data sets and~~ the ice thickness in (c) and (d) are derived from 1980-2005 global gridded data set based on European Center for Medium-Range Weather Forecast (Tietsche, et al., 2014).

带格式的：居中

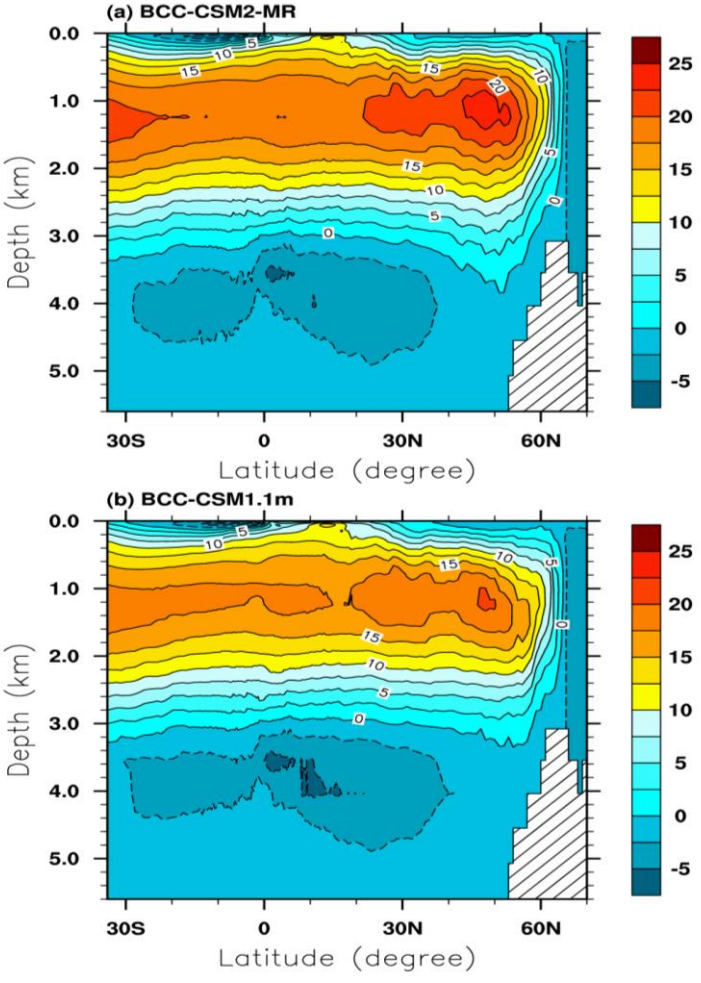


Figure 16~~9~~. Zonally-averaged streamfunction of the Atlantic Meridional Overturning Circulation (AMOC) for the period of 1980 to 2005 in BCC-CSM2-MR (top) and BCC-CSM1.1m (bottom). Units: Sv

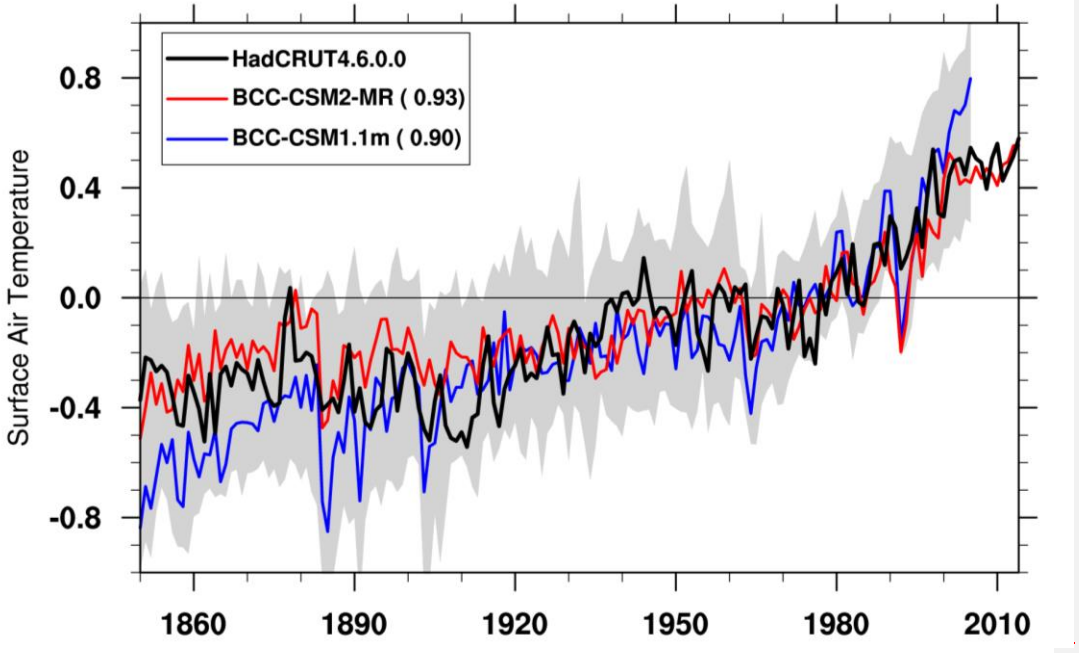


Figure 10. Time series of anomalies in the global (60 ℃S to 60 ℃N) mean surface air temperature from 1850 to 2014. The reference climate to deduce anomalies is for each individual curve from 1961 to 1990. The numbers in the bracket denote the correlation coefficient of 11-year smoothed BCC model data with the HadCRUT4.6.0.0 (Morice et al., 2012) observation. Dashed area shows the spread of CMIP5 model data.

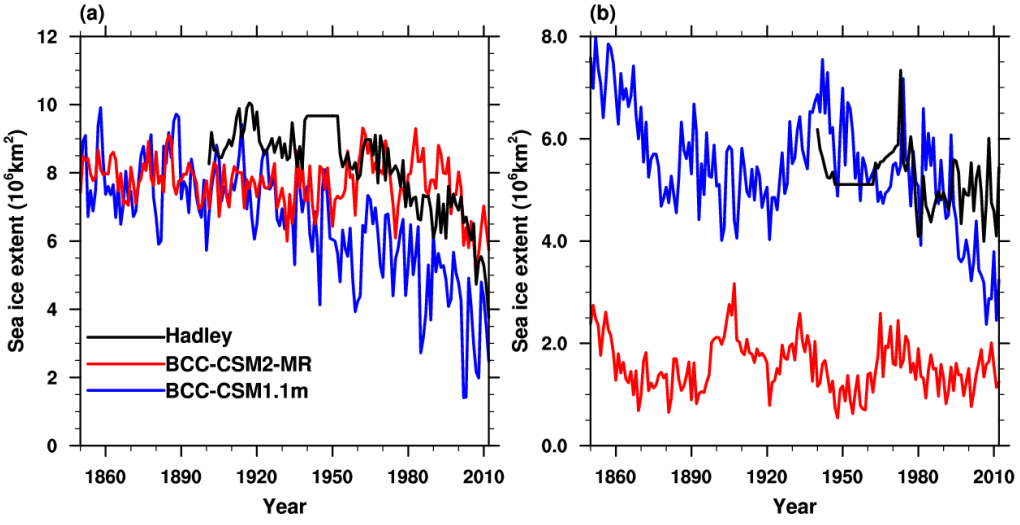


~~Figure 11. Time-series of sea-ice extent from 1851 to 2012 for (a) the Arctic in September and (b) the Antarctic in March as modelled in BCC-CSM2-MR and BCC-CSM1.1m and observations-based Hadley Centre Sea Ice and Sea Surface Temperature data set (Rayner et al., 2003).~~

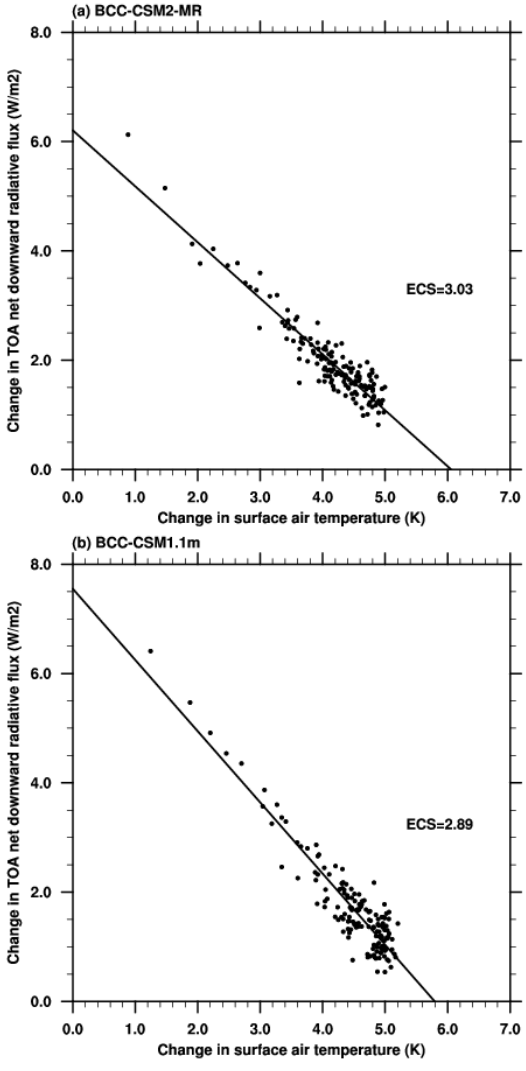


Figure 12. Relationships between the change in net top-of-atmosphere radiative flux and global-mean surface air temperature change simulated by abrupt$CO_2$ relative to the pre-industrial control run.

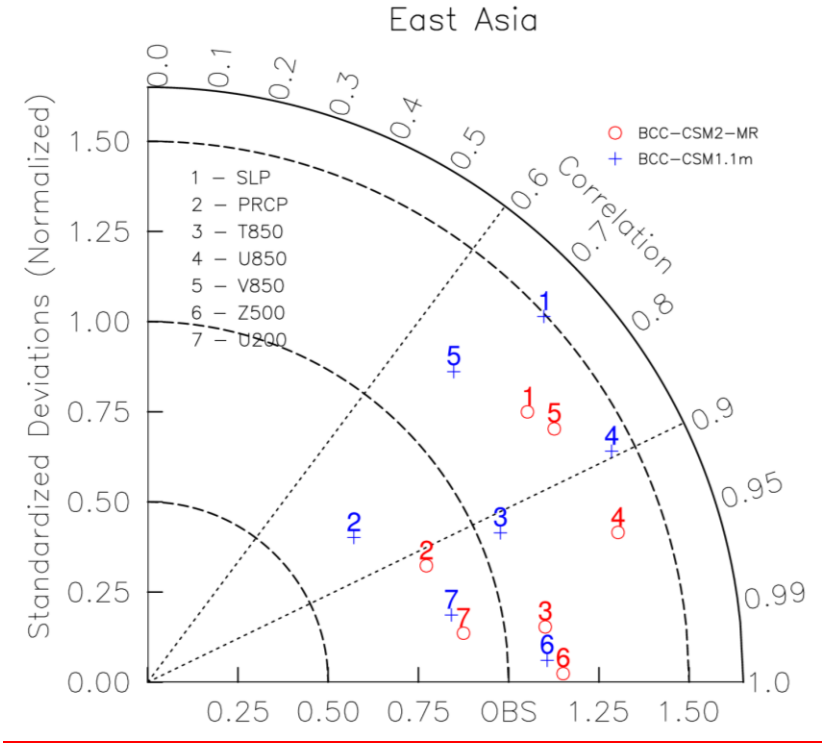
East Asia
Standardized Deviations (Normalized)
Correlation
BCC-CSM2-MR
BCC-CSM1.1m
1 – SLP
2 – PRCP
3 – T850
4 – U850
5 – V850
6 – Z500
7 – U200
0.0
0.1
0.2
0.3
0.4
0.5
0.6
0.7
0.8
0.9
0.95
0.99
1.0
0.00
0.25
0.50
0.75
1.00
1.25
1.50
0.25
0.50
0.75
OBS
1.25
1.50

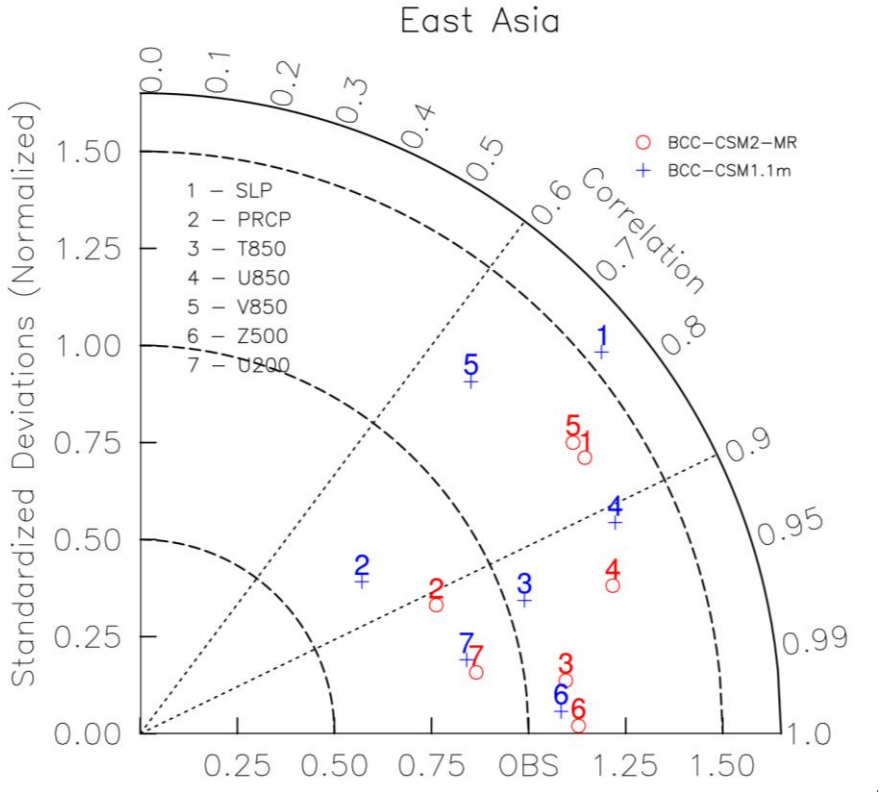


Figure 1~~7~~3. Same as in Figure 8~~4~~, but for the domain covering East Asia (20 °-50 °N, 100 °-140 °E).

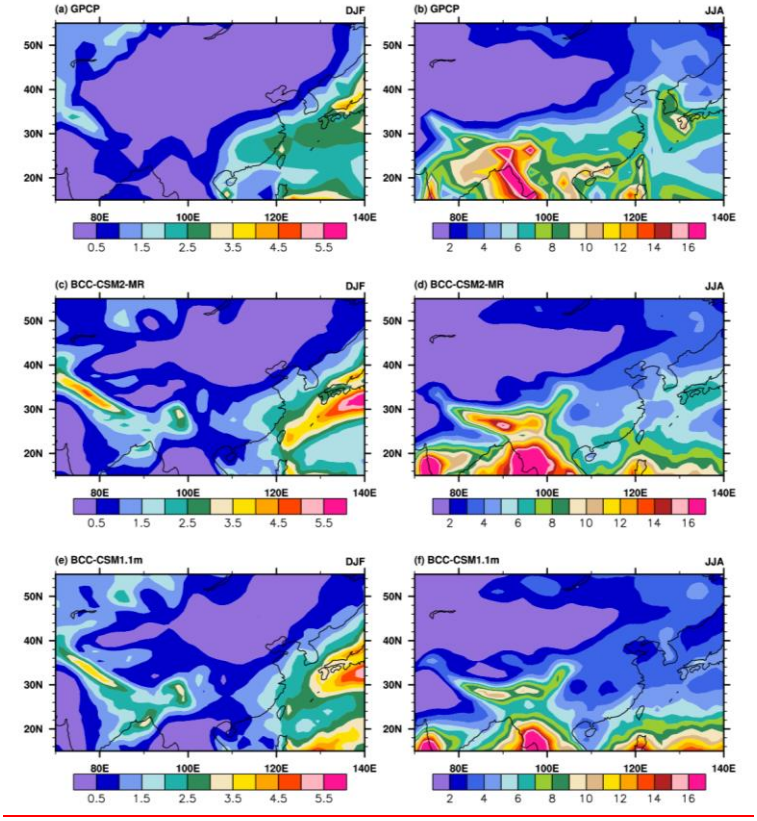


Figure 18. Regional distribution maps of precipitation climatology (averaged from 1980 to 2005) for December-January-February (left panels) and June-July-August (right panels) from (a) GPCP, (b) BCC-CSM2-MR, (c) BCC-CSM1.1m.

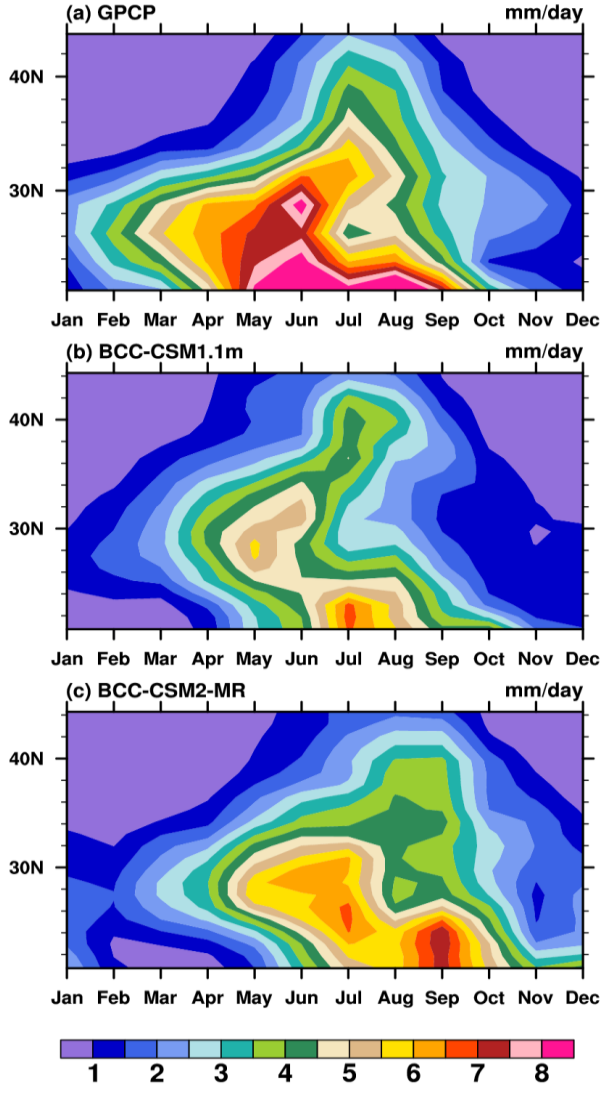
(a) GPCP
mm/day
40N
30N
Jan Feb Mar Apr May Jun Jul Aug Sep Oct Nov Dec
(b) BCC-CSM1.1m
mm/day
40N
30N
Jan Feb Mar Apr May Jun Jul Aug Sep Oct Nov Dec
(c) BCC-CSM2-MR
mm/day
40N
30N
Jan Feb Mar Apr May Jun Jul Aug Sep Oct Nov Dec
1 2 3 4 5 6 7 8

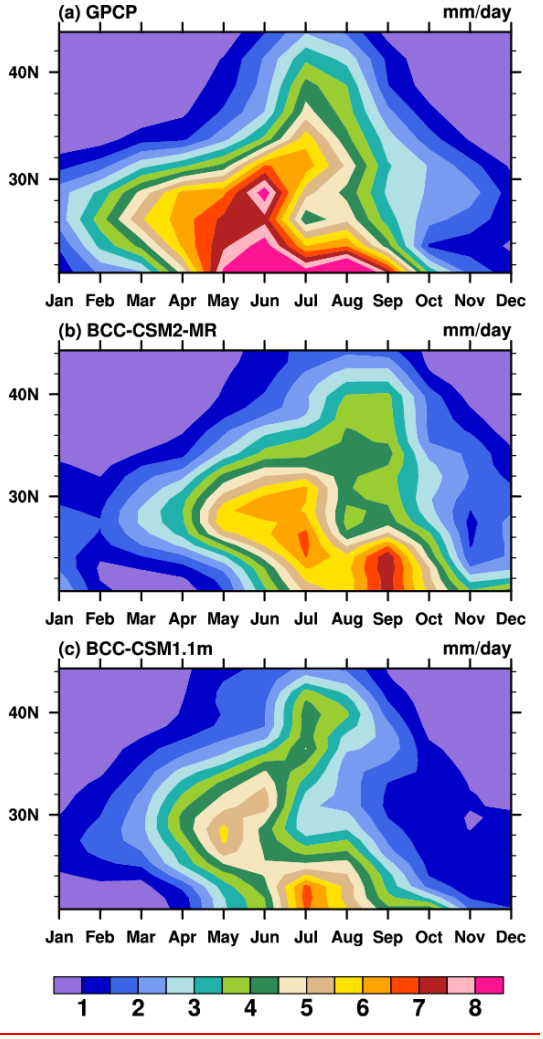


Figure 19~~14~~. L~~The~~atitude (from 20 ℃N to 25 ℃N) – month (Jan. to Dec.) diagrams showing variations of monthly precipitation averaged over 100 °-120 ℃E ~~averaged~~ and for the period of 1980-2005. ~~monthly precipitation along each latitude from 20 ℃N to 25 ℃N with time.~~ (a) GPCP, (b) BCC-CSM2-MR~~1.1m~~, (c) BCC-CSM1.1m~~2-MR~~.

带格式的：居中

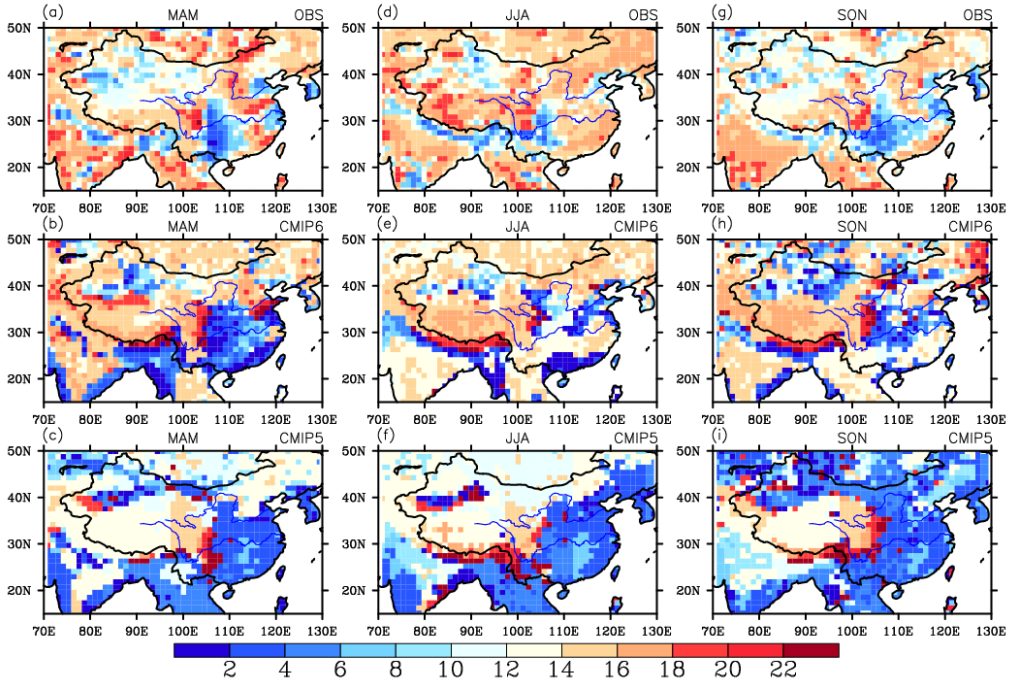


Figure 20~~15~~. Local times of maximum frequency of rainfall occurrence in March-April-May (left column), June-July-August (middle column), and September-October-November (right column) over China and its surrounding areas for BCC-CSM2-MR (middle panel), BCC-CSM1.1m (bottom panel), and TRMM data (top panel, Huffman et al., 2014). The rainfall occurrence is defined as the hourly precipitation larger than 1 mm ~~for BCC-CSM2-MR (middle panel), BCC-CSM1.1m (bottom panel), and TRMM data (top panel, Huffman et al., 2014)~~.